UNIVERSITY OF OKLAHOMA

GRADUATE COLLEGE

A STATISTICAL APPROACH TO DIAGNOSING STORM MODE

A THESIS

SUBMITTED TO THE GRADUATE FACULTY

in partial fulfillment of the requirements for the

Degree of

MASTER OF SCIENCE IN METEOROLOGY

By

DAVID STANG
Norman, Oklahoma
2021

A STATISTICAL APPROACH TO DIAGNOSING STORM MODE

A THESIS APPROVED FOR THE
SCHOOL OF METEOROLOGY

BY THE COMMITTEE CONSISTING OF

Dr. Harold Brooks, Chair

Dr. Michael Richman

Dr. Xuguang Wang

Table of Contents

Abstract

Determining storm mode (linear or isolated) is a crucial component of any severe weather forecast. Isolated storms are associated with a greater likelihood of significant (EF2+) tornadoes and very large (2”+) hail, while linear storms are more likely to produce straight-line wind damage. Current operational convection allowing models (CAMs), which are often used to diagnose storm mode, only run up to 48-60 hours into the future and can quickly lose accuracy with increasing lead time. To improve forecast accuracy and messaging on Day 3+ outlooks, a forecast tool was created to predict storm mode using only synoptic-scale variables. The approach uses a blend of theoretical modeling, stochastic modeling, and statistical modeling. The formulation generally performed well with reproducing past events and predicting future events 84+ hours in advance using 0.5° Global Forecasting System (GFS) and 0.5° Global Ensemble Forecasting System (GEFS) outputs.

I. Introduction

Isolated storms are associated with a greater likelihood of significant long-track tornadoes and linear storms are associated with a greater likelihood of widespread significant wind damage (Smith and Thompson 2012). Therefore, accurately predicting storm mode (linear or isolated) is a crucial component of any severe weather forecast.

One common forecasting tool used to diagnose storm mode is convection allowing models (CAMs), but most operational CAMs only run up to 48-60 hours in the future. Furthermore, most CAMs quickly lose accuracy with increasing lead-time (Stratman and Coniglio 2013) and can be very sensitive to initial conditions (Schwartz and Wong 2020).

Synoptic-scale and global numerical models (e.g. GFS and ECMWF) run deeper into future (384 hours for the GFS and 240 hours for the ECMWF), but the current operational grid resolution (10 km to 20 km) is too coarse to accurately and consistently resolve some small-scale phenomena, including convective mode (ECMWF 2017).

However, global models do provide information on the larger-scale environment, and this information can conceivably be used to infer storm mode. Synoptic-scale boundaries (i.e. cold fronts, warm fronts, and dry lines) provide an axis along which storms can initialize. If no boundary is present, the individual convective cells that form are, as a practical matter, randomly distributed. The background wind field can also be used to estimate the velocity (direction and speed) of any convective cells that do form. Furthermore, the degree of vertical forcing and extent of vertical (in)stability can provide information on the number of convective cells that form.

The goal of this research will be to develop a tool to predict storm mode using only synoptic-scale variables. If successful, global numerical models (e.g. GFS, ECMWF) and mesoscale numerical models (e.g. NAM) can provide a forecast for storm mode as far into the future as the model runs. The end goal of this research would be to improve the overall accuracy of medium range forecasts (made 72+ hours in advance) by quickly providing forecasters an idea on what storms modes (linear, mixed, or isolated) are favored, which would quickly provide an idea on what sort of severe weather event (i.e. tornado outbreak or squall line) might occur 72+ hours in advance. The development of an accurate model would allow the forecasting process to become more efficient, and the communication of future hazards to emergency managers and the general public could be improved.

II. Methodology

Conception

The hypothetical model to predict storm mode, known as the Convective Mode Prediction System (CoMPS), can be divided into two scenarios; a scenario in which convection develops along a well-defined boundary, and a scenario in which convection develops without a well-defined boundary (non-frontal convection). The scenario involving non-frontal convection employs the use of a stochastic model, since, as a practical matter, non-frontal convection is

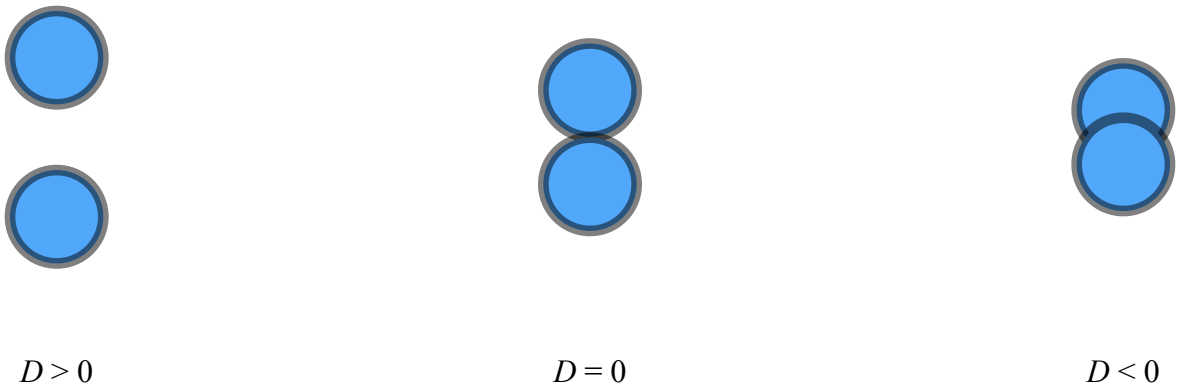

Figure 1. This figure shows how to interpret the spacing parameter D. Positive values of D imply two cold pools that do not overlap at all. A value of $D = 0$ implies two cold pools whose edges overlap. Negative values of D imply two cold pools whose interiors overlap.

randomly distributed. The scenario involving convection along a boundary will be the main emphasis for this study.

In developing CoMPS, the overall objective is to translate a storm-scale perspective into something that can be approximately reproduced from a framework that is entirely dependent on synoptic-scale variables. The below table provides an overview of all relevant quantities and how the synoptic-scale variables relate to these quantities.

Metric	Synoptic-Scale Derivate
Cell Mode	Classified as either "linear" or "isolated" by means of a graphical discriminant function that only depends on the spacing parameter D (Figure 1) between two individual cells (detailed later). If only one cell exists, the mode is 100% isolated.
Convective Cell Position	Estimated based on (1) whether or not a well-defined boundary exists and (2) the likelihood of a cell forming along the boundary. If a well-defined boundary exists, it will be assumed that individual cells form along the boundary's axis. Otherwise, individual cells will form in random locations.
Cell Velocity	LCL-EL mean wind vector (obtained via forecast soundings).

Cell Width	Empirically estimated mean (detailed later), and the individual convective cells are treated as ellipses with equivalent major and minor axes. The TITAN algorithm (Dixon and Wiener 1993), which is considered to be the gold standard for objectively identifying convective cells, uses ellipses to approximate the full extent of the storms. However, TITAN knows the exact geometry of a storm since observational data is being used. Determining the geometry of a storm using synoptic-scale variables would be a complicated process. Therefore, this will be simplified by using elliptical bounds whose major and minor axes are equivalent.

To calibrate a means of objectively identifying storm mode (linear or isolated), there must first exist a method of objectively identifying individual storm cells. The following objective radar analysis algorithm (graphically depicted in Figure A1) is designed to accomplish this specific task:

1) Scan through individual grid points on the radar base reflectivity (0.5° elevation) data. If a particular grid point's reflectivity value is at least 40 dBZ, proceed to Step 2 of this algorithm. Using the nomenclature from Dixon and Wiener 1993, 40 dBZ would be the value of T_Z (the threshold reflectivity value for identifying a feature of interest)

2) Estimate the direction of the reflectivity gradient vector ∇R.

$$\delta x = R_{x+1} - R_{x-1}$$

$$\delta y = R_{y+1} - R_{y-1}$$

Where δx represents the reflectivity value of the right-adjacent grid point minus the reflectivity value of the left-adjacent grid point, and δy represents the reflectivity value of the top-adjacent grid point minus the reflectivity value of the bottom-adjacent grid point.

Since the horizontal and vertical grid resolutions are equivalent, there is no need to divide δx and δy by the quantity $2 \cdot \Delta x$ (the x-axis grid resolution) or $2 \cdot \Delta y$ (the y-axis grid resolution).

$$\theta_R = \tan^{-1}\left(\frac{\delta y}{\delta x}\right) = \tan^{-1}\left(\frac{R_{y+1} - R_{y-1}}{R_{x+1} - R_{x-1}}\right)$$

3) Step forward along the direction of θ_R (parallel to the direction of ∇R) until a grid point's reflectivity value is less than 40 dBZ.

4) If a grid point's reflectivity value is less than 40 dBZ, plug the reflectivity value into the following equation:

$$T = \frac{40\ dBZ}{R}$$

Where R is the grid point's reflectivity value. Note that R is assigned a minimum value of 1 (primarily to avoid dividing by 0). If there is no reflectivity data available at this grid point (R is -999), the algorithm then skips to Step 6.

The value of T is added to a "tolerance variable". If the value of the tolerance variable ever exceeds 10, the algorithm will call this the edge of the storm.

Most objective radar analysis algorithms, including those found in Dixon and Wiener 1993, Peter et. al. 2015, Zan et. al. 2019, and Shah et. al. 2015; look at contiguous grid points that strictly exceed the value of T_Z (threshold reflectivity). This algorithm relaxes this rule to avoid prematurely terminating the tracing of a storm just because one grid point's reflectivity value happens to drop below 40 dBZ (T_Z), which is most often a result of random observational error.

5) If a grid point's reflectivity value is greater than 40 dBZ, the "tolerance variable" (mentioned in Step 4) is reset to 0.

6) Repeat Steps 3 - 5, allowing the original calculation for the reflectivity gradient angle θ_R (Step 2) to vary between -15 ° and +15 ° of what was originally estimated. The highest value for storm width is retained and used for Step 7, and the gradient vector angle that yielded this maximum in storm width is called θ_{max}

If a width below 10 km is estimated, the algorithm skips this potential storm and returns to Step 1. This effectively requires a storm's area be at least 78.5 km^2, which is similar to approaches used by Peter et. al. 2015 and Zan et. al. 2019. Both of these studies advocate for only considering features whose area exceeds a threshold value (30 km^2 in the case of Peter et. al. 2015 and 15 km^2 in the case of Zan et. al 2019). The larger area is used in this study, because the objective is to capture the full extent of a deep convective cell with a well sustained cold pool.

7) Based on the value of storm width from Step 6 and the original start point (from

Step 1), estimate the central point of the cell using:

$$x_{center} = x_0 + 0.5 * \Delta s * \cos \theta_{max}$$
$$y_{center} = y_0 + 0.5 * \Delta s * \sin \theta_{max}$$

where x_0 and y_0 represent the starting point from Step 1 and Δs is the cell's width.

After all of the individual storms cells have been identified, the distance between each cell's outer edge (the spacing parameter D, conceptually depicted in Figure 1) can be calculated and used to probabilistically gauge the storm mode that is present. Once a strategy has been devised to probabilistically classify storm mode based on observed radar data, the same strategy can be used to probabilistically classify storm mode using hypothetical convective cells. The specific strategy used in this study is a graphical discriminant function (GDF), the derivation and underlying details of which will be discussed in greater depth later on. First, a method will be devised to infer where individual storms would hypothetically form.

The hypothetical positions of each storm that forms along a boundary can be supposed using the probability of a storm initiating (discussed later) and the orientation (angle) of the main boundary (discussed below), if such a boundary exists.

The orientation (angle) of a "well-defined" (formalized below) boundary is determined using the following algorithm:

1) Isolate a subsection of the grid that measures approximately 1000 km × 1000 km.

2) Using temperature and dewpoint (moisture) fields in the subsection, calculate θ_e.

$$\theta_e = T \exp\left(\frac{L_v\, w}{c_p\, T}\right)$$

Where T is the air temperature (in Kelvin), L_v is water's latent heat of vaporization (2.5×10^6 J/kg), w is the water vapor mixing ratio (obtained from the dewpoint field, in units of g/g or kg/kg), and c_p is the dry air gas constant under constant pressure (1004.67 J/kg/K).

3) Using θ_e (calculated in Step 2), estimate $\nabla\theta_e$ at each grid point.

$$\nabla\theta_e = \frac{\theta_{x+1} - \theta_{x-1}}{2\,\Delta x}\,\hat{i} + \frac{\theta_{y+1} - \theta_{y-1}}{2\,\Delta y}\,\hat{j}$$

Where Δx is the grid spacing in the x-direction, Δy is the grid spacing in the y-direction, θ_{x+1} is the value of θ_e for the right-adjacent grid point, θ_{x-1} is the value of θ_e for the left-adjacent grid point, θ_{y+1} is the value of θ_e for the top-adjacent grid point, θ_{y-1} is the value of θ_e for the bottom-adjacent grid point.

4) Highlight grid points of $|\nabla\theta_e|$ that are greater than 0.8 K / km. If the number of points highlighted is less than or equal to 1, the threshold of 0.8 K / km is relaxed until multiple points are highlighted. The relaxation is obtained by multiplying the old value by 0.5. For example, if the grid yields no values of $|\nabla\theta_e|$ greater than 0.8 K / km, the next scan will look for values of $|\nabla\theta_e|$ greater than 0.4 K / km, followed by 0.2 K / km and then 0.1 K / km. If the threshold value drops below 0.1 K / km, the subsection will be labeled as having no "well-defined" boundary.

5) If more than 2 grid points are highlighted from Step 4, perform a linear regression on the highlighted grid points. The slope of the best-fit line then provides the orientation (angle) of the boundary.

6) Adhere to a predetermined convention for front angle, which is as follows: if a boundary is "pointing" in a particular direction, the air to the right of that vector should be unstable (higher θ_e) and the air to the left of that vector should be stable (lower θ_e). As an example, if a boundary is "pointing" to the northeast, unstable air (higher θ_e) should lie to the southeast and stable air (lower θ_e) should lie to the northwest.

The approach used here does not consider the wind field and combines the temperature and moisture fields into a single field (θ_e). Bitsa et. al. 2021 devised an algorithm to objectively identify cold fronts by highlighting winds shifts greater than 30° and a meridional wind component that goes from positive to negative. Bitsa et. al. 2021 also requires the zonal wind be westerly and the wind speed itself (magnitude) be at least 5 m/s. Additionally, the algorithm in Bitsa et. al. 2021 combines the wind field and temperature gradient vector to consider temperature advection at 850 mb. Most importantly, Bitsa et. al. 2021 looks at individual grid points.

CoMPS's front identification algorithm examines gradients of θ_e to identify all potential boundaries (including dry lines, which can exhibit an ill-defined temperature contrast during the daytime). Furthermore, dry lines rarely feature a southerly-to-northerly wind shift and instead

feature an easterly-to-westerly wind shift. Additionally, warm fronts often feature a gradual change in wind direction. Therefore, the process for identifying any arbitrary boundary cannot easily involve a wind shift metric as a criterion. For this reason, wind data is excluded from consideration.

Furthermore, Bitsa et. al. 2021 looks at individual grid points in a sort of microscopic perspective. CoMPS examines large subsections (measuring approximately 1000 km × 1000 km), thereby considering 256 grid points (16 grid points × 16 grid points) simultaneously (in the case of the model data used, the model details will be discussed later). This provides a more macroscopic and synoptic-scale perspective that also mitigates the impacts of problematic model grid points that are reporting errant values.

The above algorithm operates on information at the 1000 mb pressure level, but could theoretically work for any isobaric surface. While using the 1000 mb pressure level would seemingly neglect numerous observations (since many regions have elevations above the 1000 mb pressure level), the numerical model outputs involved in this algorithm will infer the temperature and dewpoint at 1000 mb. An isobaric perspective is used, because using 2-meter of 10-meter metrics could produce thermal gradients that are solely caused by differences in elevation and the not the presence of a boundary.

Once the orientation of a boundary is determined, CoMPS will initiate an array of evenly spaced hypothetical convective cells along the boundary's axis (determined from step 5 in the above algorithm). The distance between each cell is estimated based on the probability of a storm initiating (discussed later) and the area of the boundary's "initiation zone" (empirically estimated and discussed below). For a visual representation of this process, please refer to Figure A2.

To determine all empirically estimated quantities (including the aforementioned "initiation zone"), level II radar data was obtained for severe weather events from 2015-2019 that met the following criteria: (1) prompted at least an enhanced (level 3) risk from the Storm Prediction Center (SPC) and (2) featured convection that exclusively formed along or near a well-defined boundary (surface or elevated). Out of the 322 total enhanced risk events within this timeframe (SPC Severe Weather Events Archive), 187 events featured exclusive convection along a well-defined boundary. The following algorithm is combined with the objective radar analysis algorithm to estimate the size of the initiation zone.

Initiation zone algorithm:

1) Run the above objective radar analysis algorithm on radar base reflectivity (0.5° elevation) data.

2) The center point and width of each cell (from Step 1) is then estimated (also the aforementioned objective radar analysis algorithm).

3) Perform a linear regression on the central points of each cell (from Step 1), and the slope of the best-fit line represents a rough approximation of the attendant boundary's orientation. It should be noted that observations of temperature and moisture were originally intended for this step, but these measurements are taken

at either 2-meters above ground level (AGL) or 10-meters AGL. However, this runs into the same problem mentioned earlier (temperature and stability gradients caused by differences in elevation that can be misidentified as a boundary). Therefore, the axis along which the convective cells form is taken as the orientation of the main boundary.

4) For each cell, the distance between the cell's outermost edge and the boundary axis estimate (from Step 3) is calculated. The size of the initiation zone is then taken as the highest distance value obtained from this step.

5) Repeat this process for all radar data obtained. The mean initiation zone size and storm size are then used in CoMPS's algorithm when initiating hypothetical storm cells.

The data specifically used in this study produced a mean value of 35.8 km (exact number 35.84475806451613 km) for the width of a convective cell and a mean value of 140.0 km (exact number 139.99618625655287 km) for the width of a boundary's initiation zone (70.0 km ahead of the boundary and 70.0 km behind the boundary). These data also yielded a mean forward speed of 35.495 knots (40.819 mph, 65.731 kph) for a convective cell.

The intent of this approach is to determine a mean value that can be applied to any "well-defined" synoptic-scale boundary. Weckworth and Parsons 2006 recommends examining zones of boundary layer convergence that are 10 km in width. However, the intent of CoMPS is to operate on global models, which normally struggle to resolve finer-scale processes involved in boundary layer dynamics. While using some sort of convergence metric may improve accuracy and yield better consistency, determining a sensible threshold value for the magnitude of convergence will prove challenging for the following reasons:

- Strong convergence is not an automatic guarantee for initiating convection. Correlating a magnitude of convergence with convective initiation will be complicated by atmospheric stability and the degree of lifting from upper air features (e.g. differential cyclonic vorticity advection and diffluent jet streams).
- Weak convergence can initiate thunderstorms in uncapped and highly unstable warm sectors. Thunderstorms can also form due to strong heating in such environments. In such situations, it becomes unclear whether the weak convergence is attributable to convective development or the ambient vertical motions (not caused by the near-surface convergence) is attributable to convective development.

Therefore, events involving only convection along a discernible frontal axis were analyzed. From there, an analysis of the radar data can estimate the geometry and size of a synoptic boundary's initiation zone.

Now that there exists a strategy to determine both the axis of a "well-defined" boundary and the area of the boundary's initiation zone, estimating the probability of cells initiating will

complete the basis for inferring how many cells will form along the boundary's axis. Since the main ingredients for thunderstorm formation are unstable air and lift (ambient vertical velocity), the approach for estimating the probability of initiation P_0 will involve the stability of the tropospheric profile and the degree of forcing (geometric vertical velocity). If no "well-defined" boundary is detected, the hypothetical cells are randomly distributed across 256 km × 256 km area.

To estimate P_0, data from the deterministic 0.5° Global Forecasting System (GFS) and the 30 individual members of 0.5° Global Ensemble Forecasting System (GEFS) were used. The timeframe examined coincides with the convective outlook timeframe utilized by the Storm Prediction Center, which is 12Z from the day of a severe weather event to 12Z on the next day. Each timestamp from the GFS and GEFS outputs is a 3-hour time span (a time window consistent with Dial. et. al. 2010), yielding a total of 9 different forecast hours from both GFS and GEFS (including the 12Z data on the day following a potential severe weather event). The value for P_0 is then calculated using the following algorithm:

1) Isolate a 256 km × 256 km subsection on the model grid and calculate a horizontal mean of the vertical temperature, moisture, and pressure profiles queried from each grid point in the subsection.

2) In the same subsection from Step 1, determine the maximum vertical velocity present in the atmospheric column (limited to altitudes below 100mb). Multiplying this value by 0.5 yields an estimate for a representative vertical velocity in the column. The mean of all representative vertical velocities in the subsection is then calculated and applied to each grid point in the subsection.

3) Using individual ensemble members (from the Global Ensemble Forecasting System, GEFS), determine an uncertainty term for temperature σ_T by calculating the standard deviation of temperature between each ensemble member. The value of σ_T is then multiplied by a gain of 1.414, a number that is obtained by means of ensemble member dressing (Wang et. al. 2004).

4) Using the deterministic model (the Global Forecast System, GFS), determine the variance of the geometric vertical velocity between each vertical grid point. The square root of this variance yields an uncertainty term for vertical velocity σ_w. Note that GEFS assumes hydrostatic balance, meaning there is no direct vertical velocity data from the individual ensemble members. Therefore, an uncertainty value must be obtained using only the deterministic model output. The value of of σ_w is then multiplied by a gain of 1.414, a number that is obtained by means of ensemble member dressing (Wang et. al. 2004).

5) Calculate the virtual temperature of a 100 mb mixed layer air parcel. Note the result obtained in Step 2 is used for the mixed layer air parcel's vertical velocity.

6) Estimate the height of the tropopause using the following algorithm:

6.1) Starting at the second lowest altitude with available temperature data, check if the temperature at this altitude is greater than the vertical grid point below it.

6.2) If the temperature has increased with height, the following quantity is calculated and added to a "tolerance variable":

$$E = \frac{T_z}{T_{z-1}}$$

Where T_z is the temperature at the height currently being queried and T_{z-1} is the temperature at the grid point directly below the height level z. Note that all temperature values in the above equation are in Kelvin.

If the "tolerance variable" exceeds 3 at any point during this algorithm, the algorithm is terminated, and the height at which the temperature first began to increase is called the tropopause height.

Of the different techniques outlined in Ivanova 2013, this technique is most similar to the "thermal tropopause" approach, in which an algorithm detects a consistent change in temperature trend over a contiguous layer in the lower atmosphere. However, CoMPS's algorithm is looking for temperatures that steadily increase with height while Ivanova 2013 looks for a specific lapse rate value (2 °C / km or lower). Other potentially relevant techniques include the "static stability criterion", which highlights changes in the Brunt Väisälä frequency; the "cold point tropopause", which looks for a minimum temperature in the vertical profile; and the "dynamical tropopause", which looks for an Ertel potential vorticity of 1-4 Potential Vorticity Units (PVU).

Most of the scientific literature reviewed in the study (including Lewis 2009, Rao et. al. 2007, Xia et. al. 2020, and Pan et. al. 2013) use data that is exclusively observational in nature. Both Lewis 2009 and Rao et. al. 2007 identify the tropopause using GPS Radio Occultation (RO) while Xia et. al. 2020 advocates using a "refractivity profile". Pan et. al. 2013 uses a method combining observations of ozone, water vapor, stability, and temperature to identify the tropopause. Until numerical models are able to accurately reproduce such phenomena, atmospheric variables must be used. Since the chief concern for this aspect of CoMPS is the stability of air parcels (and not the stability of the ambient tropospheric air), a more

direct and straightforward technique involving changes in vertical temperature was adapted for use in this study. However, an avenue for future work could involve a detailed comparison of forecast performance using different tropopause identification techniques.

6.3) If the temperature decreases with height at any point, the "tolerance variable" is reset to 0.

6.4) Repeat steps 6.1 through 6.3, increasing altitude until the tropopause height is obtained.

6.5) Once the height of the tropopause is estimated, limit the tropopause height to a value within the range of 6000 meters and 10000 meters. This is done to prevent the algorithm from misidentifying a substantial low-level inversion as the tropopause. If the tropopause height is greater than 10000 meters, the air mass is likely tropical in nature and the parcels do not need to reach the top of the troposphere to form convective cells.

The tropopause height is used in lieu of equilibrium level (EL), because this algorithm will involve changing the mixed layer parcel's initial temperature (Step 13), which will also change the height of the EL. To maintain consistency, a fixed height (predetermined based on the environmental temperature profile) is used a benchmark to gauge the stability of mixed layer air parcels.

7) Give the mixed layer air parcel a small vertical displacement equivalent to $w \times (0.1\ s)$ above the median pressure level (e.g. mixing an air parcel using properties in the 1000 mb-900 mb layer will situate the parcel slightly above 950 mb), where w is the parcel's initial vertical velocity (estimated in Step 2). The mixed layer parcel is used since the primary concern is convective initiation and the not the maintenance of ongoing convection.

8) Using linear interpolation, estimate the ambient temperature and ambient pressure at the air parcel's altitude.

$$\overline{T} = \left(\frac{T_j - T_i}{z - z_i} \right) \left(z - z_i \right) + T_i$$

$$\overline{P} = \left(\frac{P_j - P_i}{z - z_i} \right) \left(z - z_i \right) + P_i$$

9) Using the parcel's temperature and ambient temperature (from Step 8), calculate the buoyant force experienced by the parcel and the acceleration experienced by the air parcel (using a time increment of 1.0 seconds).

$$a_{n+1} = a_n + g_0 \left(\frac{T'}{\bar{T}} - 1 \right) \Delta t$$

10) Using the acceleration (from Step 9), calculate a new vertical velocity for the air parcel (using a time increment of 1.0 seconds).

$$w_{n+1} = w_n + a_{n+1} \Delta t$$

11) Using the new vertical velocity (from Step 10), calculate the new altitude of the air parcel (using a time increment of 1.0 seconds).

$$z_{n+1} = z_n + w_{n+1} \Delta t$$

12) Using the change in altitude (obtained from Step 11), determine the change in parcel temperature. If the air parcel is unsaturated, the parcel's temperature decreases at a rate of 9.8 K / km. If the air parcel is saturated, the parcel's temperature decreases at the moist adiabatic lapse rate (using the ambient pressure, from Step 8, and the parcel's temperature).

$$T_{n+1} = T_n - \gamma \left(z_{n+1} - z_n \right)$$

Where γ represents the parcel's lapse rate.

13) If the parcel reaches the tropopause (from Step 6), decrease the air parcel's virtual temperature by 0.1 K and repeat Steps 7-12 until a virtual temperature causes the parcel to become stable. This result becomes the "critical virtual temperature" T_v*. Otherwise, if the parcel fails to reach the tropopause, increase the air parcel's virtual temperature by 0.1 K and repeat Steps 7-12 until a virtual temperature causes the parcel to become unstable. This result becomes the "critical virtual temperature" T_v*. Note that this holds the initial vertical velocity constant and only manipulates the parcel's initial virtual temperature.

14) Once T_v* is determined, repeat a similar process for vertical velocity w. If the air parcel reaches the tropopause (from Step 6), decrease the air parcel's vertical velocity by 0.01 m/s and repeat Steps 7-12 until a vertical velocity causes the parcel to become stable. This result becomes the "critical vertical velocity" w*. Otherwise, if the parcel fails to reach the tropopause, increase the air parcel's vertical velocity by 0.01 m/s until an initial vertical velocity causes the parcel to become unstable. This result becomes the "critical vertical velocity" w*. Note that this holds the initial virtual temperature constant and only manipulates the parcel's initial vertical velocity.

15) Once T_v* and w* are determined, calculate the below probabilities using the model's forecast for a mixed layer parcel's virtual temperature and initial vertical velocity.

$$P_T = \frac{1}{\sigma_T \sqrt{2\pi}} \int_{-\infty}^{T_v} \exp\left(-\frac{1}{2}\left(\frac{T_v - T_v^*}{\sigma_T}\right)^2\right) dT_v$$

$$P_w = \frac{1}{\sigma_w \sqrt{2\pi}} \int_{-\infty}^{w} \exp\left(-\frac{1}{2}\left(\frac{w - w^*}{\sigma_w}\right)^2\right) dw$$

16) The initiation probability P_0 then becomes the mean of P_T and P_w. A "high" value of P_0 would be greater than 0.1 (10 %). The estimation of P_0 is intended to resemble a Bayesian approach, and Kawabata and Ueno 2020 uses a Bayesian approach to estimate the probability of convective initiation. However, CoMPS estimates error terms by exclusively using ensemble members and dressing the individual ensemble outputs. Kawabata and Ueno 2020 use a combination of predetermined Gaussian errors and ensemble errors.

Furthermore, the values for P_0 are intended to represent 256 km × 256 km areas, which is an extremely coarse grid resolution when compared to Kawabata and Ueno 2020 (which uses 2 km and 15 km grids) and Pinto et. al. 2006 (which uses 4 km and 20 km grids).

Since there now exists a collection of algorithms to identify "well-defined" synoptic-scale boundaries (if they exist), the orientation (angle) of synoptic-scale boundaries, and the probability of convective cells initiating along this boundary; there is now a theoretical framework for initiating an array of hypothetical convective cells along a synoptic-scale

boundary. The final component of this predictive model is an objective method for mathematically classifying the mode (linear or isolated) of hypothetical (and observed) cells.

A graphical discriminant function (GDF) was employed to classify individual cells as "linear" or "isolated". The GDF is a method to probabilistically categorize a quantity by only considering one parameter. In this case, the lone parameter is the spacing parameter D. Deriving the GDF requires calculating the mean μ and standard deviation σ of datasets where the categorization is known. Once this is accomplished, the values of μ and σ are used to generate probability distribution functions (PDFs) for the two categories involved (in this case, a linear storm mode or an isolated storm mode). The PDFs are based on normal distributions, whose cumulative distribution functions (CDFs) are given below.

$$x_{isolated} = \frac{1}{\sigma_{isolated}\sqrt{2\pi}} \int_{-\infty}^{D} \exp\left(-\frac{1}{2}\left(\frac{D - \bar{D}_{isolated}}{\sigma_{isolated}}\right)^2\right) dD \tag{1a}$$

$$x_{linear} = \frac{1}{\sigma_{linear}\sqrt{2\pi}} \int_{D}^{\infty} \exp\left(-\frac{1}{2}\left(\frac{D - \bar{D}_{linear}}{\sigma_{linear}}\right)^2\right) dD \tag{1b}$$

Calibrating the GDF involved acquiring individual radar images that showed purely isolated storms or purely linear storms (as determined by a human observer). The same objective radar analysis algorithm then identified the central points and widths of each storm, which are then used to calculate the values of D between neighboring storms. The values for D were then used to calculate respective values for μ and σ, thereby deriving probability distribution functions (PDFs) and cumulative distribution functions (CDFs) for linear modes and isolated modes.

The likelihood of two storms being in a particular configuration (linear or isolated) given a spacing parameter value D is determined by calculating the following integrals and then dividing by the sum of the two values.

$$r_{linear} = \frac{x_{linear}}{x_{linear} + x_{isolated}} \times 100\ \% \tag{2a}$$

$$r_{isolated} = \frac{x_{isolated}}{x_{linear} + x_{isolated}} \times 100\ \% \tag{2b}$$

An example calculation for D = 10 km: x_{linear} = 0.034 and $x_{isolated}$ = 0.336 (the exact numbers were rounded to three decimal places). The probability of being linear r_{linear} = (0.034) / (0.034 + 0.336) = 0.092 and the probability of being isolated $r_{isolated}$ = (0.336) / (0.034 + 0.336) = 0.908. Therefore, a spacing parameter D value of 10 km would suggest a high likelihood (90.8 %) of the two storms being isolated. If only one storm is involved, the storm is 100% isolated.

Implementation

Combining all of these algorithms into a single operation enables CoMPS to initiate a hypothetical array of convective cells along any "well-defined" boundaries that are identified. When CoMPS initiates a hypothetical array of convective cells, the individual cells will trace out a cold pool of diameter of Δs that is assumed to be constant. As time progresses, the individual cells move along the mean wind vector, a process modeled by the below equations.

$$D(t) = \sqrt{(x_i - x_j)^2 + (y_i - y_j)^2} - \frac{1}{2}\Delta s_i - \frac{1}{2}\Delta s_j \tag{3a}$$

$$x_i = x_{i_0} + v_i\, t \cos\theta_i \tag{3b}$$

$$x_j = x_{j_0} + v_j\, t \cos\theta_j \tag{3c}$$

$$y_i = y_{i_0} + v_i\, t \sin\theta_i \tag{3d}$$

$$y_j = y_{j_0} + v_j\, t \sin\theta_j \tag{3e}$$

Where the subscripts i and j represent two different cells that are closer to each other than any other pair of cells, Δs is the width of a cell cold pool, x is the central x-coordinate of a cell, and y is the central y-coordinate of a cell. Figure A3 shows a visual representation of this process.

Note that this quantity is dependent on time and can be negative, and, if negative, implies two storm cold pools are overlapping (Figure 1). Assumptions made when performing this calculation include:

- Cell cold pools are quasi-circular and have the same constant diameter Δs.
- Cell cold pool temperature is approximately constant.
- All cells and their attendant cold pools have the same approximate width.
- Cell velocities are constant (speed and direction are constant).

These assumptions eliminate a time dependency in the Δs terms, however, the central positions of each cell are allowed to vary with time.

Critical Spacing Parameter Value D^* (between two individual storms) is the minimum distance between two cell cold pools, which occurs at time t^*.

$$t^* = \frac{x_{i0} - x_{j0}}{v_j} \cos\theta_j + \frac{y_{i0} - y_{j0}}{v_j} \sin\theta_j \tag{4}$$

$$D^* = D(t^*) \tag{5}$$

Equation (4) is obtained by holding storm i at a constant position and taking the derivative of equation (3a) with respect to time, setting the derivative equal to 0, and solving for time t. This minimum value for D is then plugged into the GDF to probabilistically diagnose storm mode as time progresses. Eventually, at time t^*, the spacing parameter D between individual cold pools will attain a constant minimum value. This minimum value of spacing parameter is D^*, and the probabilistic storm mode (result from plugging D^* into the GDF) is the quantity plotted on forecast maps.

Figure A4 provides a schematic illustrating how CoMPS uses initiation probability P_0, initiation area A, and the front orientation angle to initiate a hypothetical array of convective cells. Estimating the number of storms to initiate and consequently the distance between individual cells is accomplished by utilizing the following process and set of equations:

1) Calculate the slope of the "well-defined" frontal boundary (if it exists).

$$m = \tan\theta_F$$

2) Using the slope of the frontal boundary, calculate the radial value of the initiation zone.

$$R = \sqrt{\left(\frac{\Delta Y}{m}\right)^2 + \left(\Delta Y\right)^2}$$

Where ΔY is the initiation zone width (empirically determined to be ~140 km)

3) The distance between each hypothetical cell (using the above value of R) is given by:

$$r = \frac{\pi R}{A P_0} \left(\frac{\Delta s}{2}\right)^2$$

Where A is the initiation zone area (taken as ΔY multiplied by 240 km), P_0 represents the initiation probability, and Δs is the width of cell (empirically determined to be ~36 km).

4) The number of storms formed within the initiation zone is given by:

$$n = 1 + \frac{R}{r}$$

If the above quantity (R / r) is less than 0.5, CoMPS will not plot a storm mode forecast since the expectation is for no storms to form. Otherwise, the value of n is rounded to obtain an integer, which is an estimate for the number of storms expected to form.

5) Initiate a hypothetical array of convective cells with a distance of r between the central points of each cell.

$$x_i = x_0 + i\, r \cos \theta_F$$

$$y_i = y_0 + i\, r \sin \theta_F$$

Where θ_F is the angle of the "well-defined" boundary, and i represents the index of the storm in question (the values of i start at 0 and go up to and including $n - 1$). The value of x_i represents the initial x-coordinate of storm number i and y_i represents the initial y-coordinate of storm number i

Non-frontal Convection

For convection that does not initiate along a well-defined boundary, a stochastic function was derived using the aforementioned framework, but with storms randomly distributed across a 256 km × 256 km area. The stochastic function was generated using the following procedure:

1) Randomly position n storms within the hypothetical 256 km × 256 km area and calculate the value for P_0 that would produce n storms in this area.

2) Using the mean wind speed obtained earlier (35.495 knots, 40.819 mph, 65.731 kph), calculate the values for D^* and t^* within a 3-hour time window. Note that

since all storms are randomly distributed and moving in the same direction, the values of t^* and D^* are independent of direction θ.

3) Plug the value of D^* from Step 2 into the graphical discriminant function to probabilistically calculate storm mode.

4) Repeats Steps 1-4 10,000 times (thereby running 10,000 trials) and calculate the mean storm mode values yielded by having n non-frontal convective cells.

5) Increase n by 1 and repeat Steps 1-5 until $n = 15$. With 14 storms, the hypothetical distribution becomes nearly 100% linear and featuring more than 14 convective cells essentially becomes 100% linear.

This algorithm generates a table of values (Table B1), which represents the stochastic function CoMPS utilizes for convection that does not initiate along a well-defined boundary. The function itself is only dependent on the value of P_0, and linear interpolation is used to estimate storm mode for values that are not exactly equal to the P_0 values calculated in the above algorithm. A graph of this stochastic function can be found in Figure A5.

Verification

The forecast accuracy of CoMPS was evaluated using two methods. The first method assessed how accurately CoMPS reproduced past severe weather events (a time dependent approach). The second method involved forecasting storm mode for future severe weather events (a time independent approach).

Observational data, including radiosonde data and level II radar data, were obtained for all SPC enhanced risk, moderate risk, and high risk days that featured convection developing along a well-defined boundary (187 events examined out of 322 total events). The LCL-EL mean wind vector was calculated from the nearest radiosonde observation site at a point in time closest to convective initiation. The value for P_0 was retroactively estimated based on the following algorithm:

1) Using the objective radar analysis algorithm, identify each individual cell depicted on a radar image.

2) Perform a linear regression on the individual cell positions identified in Step 1.

3) Calculate the residual errors for each cell using the best-fit line in Step 2.

4) Calculate the mean and standard deviation of the residual errors obtained in Step 3.

5) Calculate the z-score of each residual error obtained in Step 3.

$$z_i = \frac{x_i - \overline{x}}{\sigma}$$

6) Remove any cells whose | z | exceeded 2.0 and repeat Steps 2-5 until a linear regression yields no cells with a z-score greater than 2.0 or less than -2.0. This will objectively distinguish between cells that formed along a boundary and cells that formed ahead of a boundary. Since this part of the verification process is intended to focus on the frontal convection, there must be an objective means of disregarding the irrelevant data.

7) Calculate the area of the initiation zone and the total area of each individual cell. The value of P_0 is taken as the sum of all cell areas divided by initiation zone area.

8) Repeats Steps 1-7 on each radar image that features at least 1 discernible convective cell. The value for P_0 representing the entire event is taken as the mean of all individual P_0 values.

The radar objective analysis algorithm will probabilistically estimate the storm mode (linear or isolated) using the graphical discriminant function (GDF) and the spacing parameter D between each discernible convective cell. The CoMPS model will then use the relevant parameters (derived from the available observational data) and produce a time-dependent forecast of storm mode. The CoMPS forecast of storm mode and the observed storm mode are then compared to assess accuracy (see Section III: Results and Discussion).

To evaluate accuracy as a forecast tool (using numerical model data instead of observational data), model grids from the 0.5° Global Forecasting System (GFS) model and the 0.5° Global Ensemble Forecasting System (GEFS) model were obtained from NOMADS. Whenever the Storm Prediction Center issued a Day 4+ outlook area, the model data for the highlighted day was obtained, and CoMPS produced a forecast using the last model data a forecaster would have seen prior to issuing the Day 4+ outlook (the 00Z model suite). Since the Storm Prediction Center only issues forecasts for the Contiguous United States (CONUS), model data within a latitudinal domain of 13.0 °N - 60.5 °N and a longitudinal domain of 49.0 °W - 152 °W was used. This yielded an operational grid of 206 longitudinal coordinates by 96 latitudinal coordinates.

Evaluating CoMPS as a forecast tool involved obtaining level II data from radars that witnessed severe thunderstorms. To determine a representative forecast for the radar's coverage area, the mean storm mode forecast was calculated for a 250 km × 250 km area centered over the radar. This was then compared to the mean storm mode that the radar objective analysis

determines over 3-hour timeframes (either 12Z - 15Z, 15Z - 18Z, 18Z - 21Z, 21Z - 00Z, 00Z - 03Z, 03Z - 06Z, 06Z - 09Z, or 09Z - 12Z).

To maintain consistence, individual radar data was used instead of composite data. There exist several different techniques for combining individual radar scans into a composite, which can result in differing depictions of the ongoing thunderstorm activity. For this reason, data from individual radars was used to maintain a high degree of consistency.

To assess the accuracy of the numerical guidance (GFS and GEFS), the GFS 0-hour analysis and 3-hour forecast was obtained for the 12Z, 18Z, 00Z, 06Z runs performed on the day of the severe weather event. This serves as a "verifying observation" that can easily be compared to the numerical model data involved in the CoMPS forecast. The main purpose of this is to determine whether a CoMPS forecast is inaccurate because of substantial errors in the GFS/ GEFS outputs or a flaw in CoMPS's framework. Model data with the same grid resolution is used for the purpose of simplicity and the fact that the current upper air observation network in the Contiguous United States is very sparse (and therefore can easily miss important details).

Based on the approach used to address the task of predicting storm mode, CoMPS should perform well in severe weather events that meet the following criteria:

- Events primarily driven by synoptic-scale features (as opposed to events driven by mesoscale or microscale features). If smaller scale features play an important role in a severe weather event, the global model outputs may contain significant errors, which could conceivably translate to a CoMPS forecast that contains significant errors.
- Events whose convective cells have a width comparable to the empirically estimated mean value of 35.8 km. If observed convective cells are considerably smaller than 35.8 km, CoMPS will overestimate the potential for linear modes. If observed convective cells are considerably larger than 35.8 km, CoMPS will overestimate the potential for isolated modes.
- Events that do not feature outflow dominant convection (causing the bounds of a cold pool to exceed the cell width Δs).
- Events where storm-scale processes are negligible. A large quantity of storm splits and/or cell mergers would produce chaotic behavior that this synoptic-scale approach cannot possibly resolve.

III. Results and Discussion

CoMPS Accuracy

It should be noted that 163 events (from method one) were omitted due to either discrepancies highlighted on the objective radar analysis algorithm or substantial observational errors (thereby examining a total of 24 events). For example, a cell merger (the process of two individual cells colliding and merging into a single storm) caused an errant spike in the percentage of linear modes before reverting back to being primarily isolated (Figure A6). Since it is currently impossible for CoMPS to reproduce or forecast such storm-scale phenomena (or any

chaotic behavior), some events were omitted. Additionally, some events were omitted due to bad or misrepresented observational data (Figure A7). For instance, the nearest radiosonde may be behind a stabilizing boundary (e.g. cold front) where a pronounced wind shift would heavily skew the LCL-EL mean vector. In such situations, the forecasted direction of each storm's motions would significantly differ from what was observed. Any substantial discrepancies or errors noted on the observational data obtained also led to omissions.

The reanalysis of prior severe weather events produced a median error of 8.0 % with a 0.2 % bias (equation 6) towards linear modes. That is to say, when reproducing past events, CoMPS slightly forecasted more linear modes than were observed. Given the low median error and small bias, CoMPS generally performed well in this particular verification assessment.

$$\varepsilon = \sum_{i=1}^{N} x_i - y_i \tag{6}$$

In the above equation, x_i represents the ith forecast that corresponds to the observation y_i. Summing over all pairs of forecast and observation yields the value of bias ε.

The evaluation of CoMPS forecasts for future events (method two, see Table B2 for a complete list of the events included and the excluded events) produced a median error of 24.39 % with a 1.16 % bias towards isolated modes. The large error could be attributed to inaccuracies in the GFS and the GEFS model outputs, or it could be attributed to flaws in CoMPS implementation. This will be discussed in greater depth later on.

Table 1. These tables show a classic 2×2 contingency table for forecasts of linear modes and forecasts of isolated modes. The top table represents the individual events (one for each WSR-88D radar involved in all examined severe weather events) and the bottom table represents events weighted to the mean number of storms evolved. The symbol *a* represents the number of a times linear (isolated) modes were observed when linear (isolated) modes were forecasted (correct forecasts). The symbol *b* represents the number of times linear (isolated) modes were forecasted, but not observed (false alarms). The symbol *c* represents the number of times linear (isolated) modes were observed, but not forecasted (missed events). The symbol *d* represents the number of times linear (isolated) modes were not forecasted and were not observed (correct nulls).

Linear	Observed	Not Observed
Forecasted	a_L	b_L
Not Forecasted	c_L	d_L

Isolated	Observed	Not Observed
Forecasted	a_I	b_I
Not Forecasted	c_I	d_I

Linear	Observed	Not Observed
Forecasted	a_{LW}	b_{LW}
Not Forecasted	c_{LW}	d_{LW}

Isolated	Observed	Not Observed
Forecasted	a_{IW}	b_{IW}
Not Forecasted	c_{IW}	d_{IW}

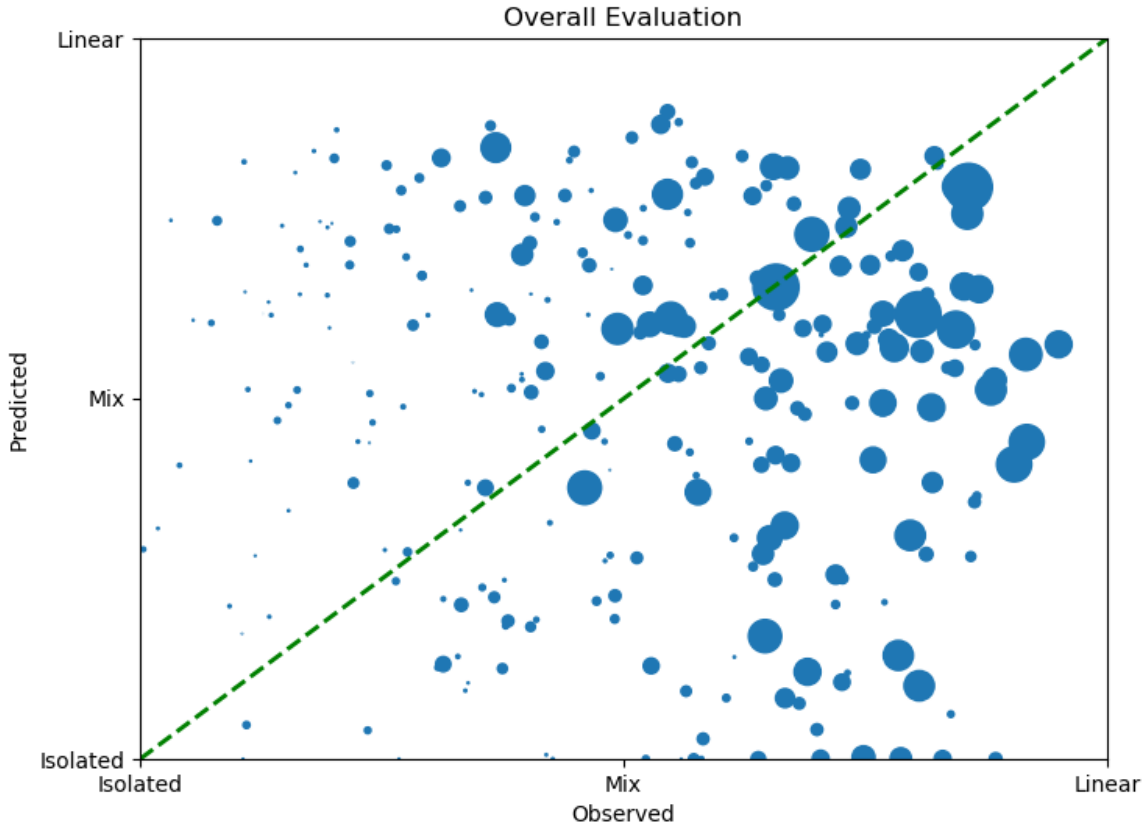

Figure 2. This figure plots predicted storm mode on the y-axis and the corresponding observed storm mode on the x-axis. The values on the axes represent the predicted or observed percentage of linear modes. For example, an ordered pair (x, y) of (0.7, 0.6) would represent an observation that is 70% linear (30% isolated) and a prediction that is 60% linear (40% isolated). If every point fell on the green dashed line, every forecast would be perfect. The size of the point represents the number of storms involved in a particular radar scan with larger circles translating to more storms.

Figure 2 shows another approach used to evaluate CoMPS forecasts. The x-axis shows the storm mode that was observed (based on the objective radar analysis). The CoMPS forecast is plotted on the y-axis. The size of each point corresponds to the mean number of storms featured in a particular severe weather event (larger points indicate more storms). The green dashed line represents where the points would be if the forecast is "perfect". A slight majority of larger points are clustered around the green dashed line, suggesting CoMPS is producing accurate forecasts for events that feature large quantities of storms. However, there is a significant number of larger points that lie far away from the green dashed line, suggesting some degree of substantial inaccuracy.

A more discretized evaluation involved placing the individual forecasts and observations into bins (essentially classifying them as either "isolated" or "linear"). If a forecast or

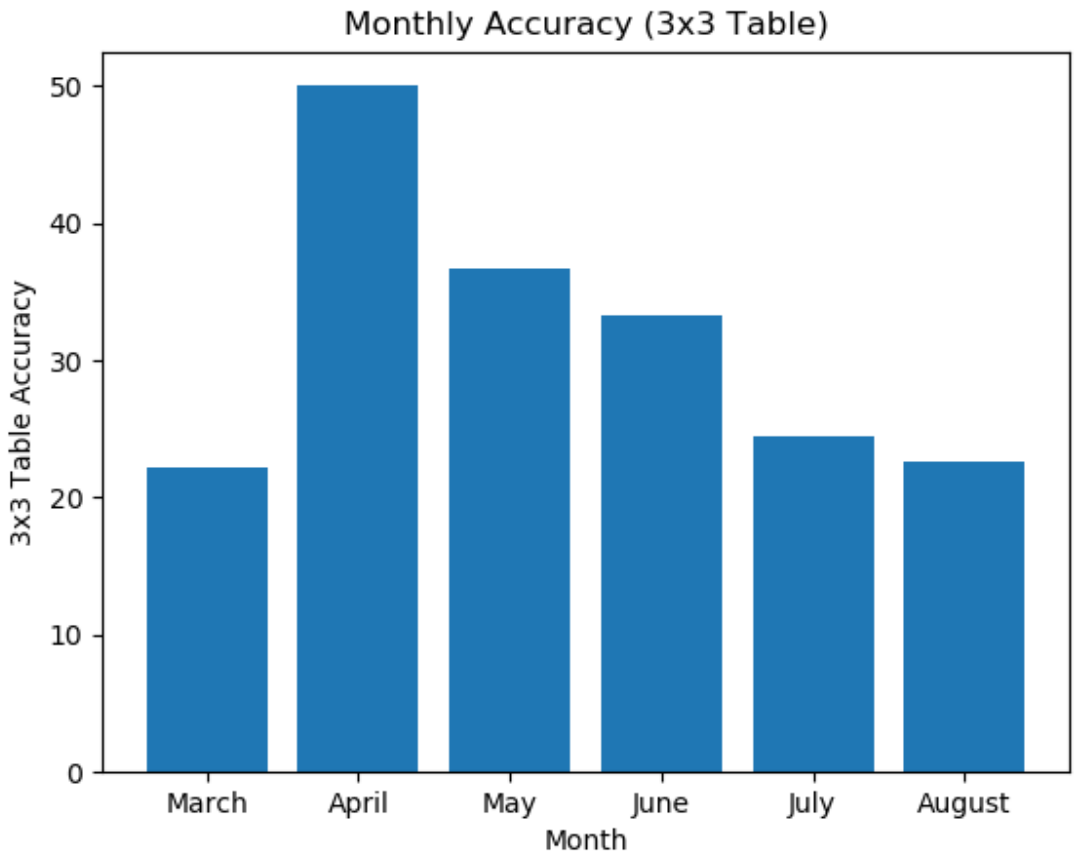

Figure 3. For the events analyzed in this study, this graph shows how accurate the CoMPS forecasts were for each month examined. Note that this shows the results of a 3x3 contingency table in which the categories are "Isolated" (33% - 100% isolated), "Mixed" (33% isolated - 33% linear), and "Linear" (33% - 100% linear). This indicates CoMPS was most accurate during the spring months, particularly in the month of April.

observation is more than 50% isolated, that forecast or observation is classified as "isolated", and a forecast or observation that is more than 50% linear is classified as "linear". This translates a continuous dataset into a classic 2×2 contingency table. This approach yielded an overall forecast accuracy of 49% (equation 7a and Table 1), but when the individual events are weighted according to the mean storm quantity, the overall forecast accuracy is 54% (equation 7b and Table 1). This would suggest that CoMPS performs better during events that feature large quantities of storms.

$$A = \frac{a_L + d_L}{a_L + b_L + c_L + d_L} = \frac{a_I + d_I}{a_I + b_I + c_I + d_I} \tag{7a}$$

$$A_W = \frac{a_{LW} + d_{LW}}{a_{LW} + b_{LW} + c_{LW} + d_{LW}} = \frac{a_{IW} + d_{IW}}{a_{IW} + b_{IW} + c_{IW} + d_{IW}} \tag{7b}$$

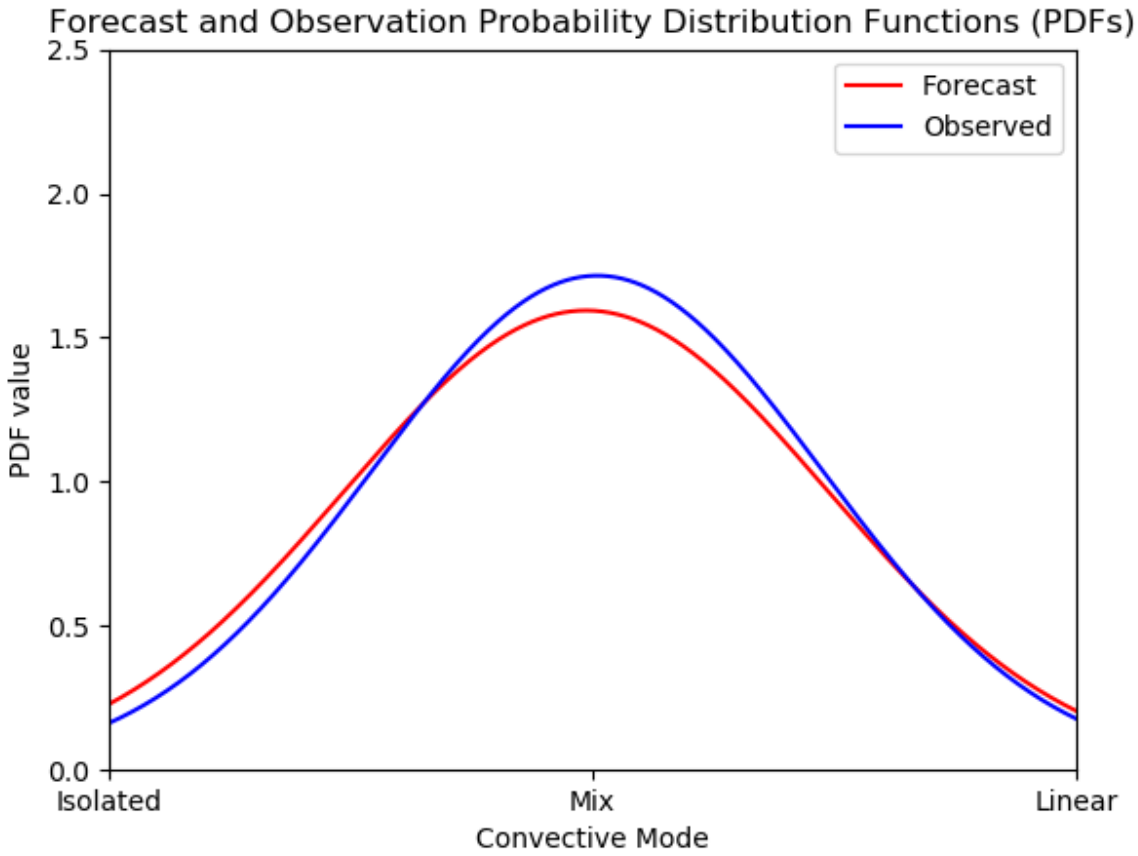

Figure 4. This figure shows the probability distribution curves for forecasted storm modes and observed storm modes. Values that tend toward the right-hand side of the graph indicate linear modes are dominant, and values that tend toward the left-hand side of the graph indicate isolated modes are dominant. Note that the forecast curve rises above the observation curve in (primarily) the isolated mode regime, suggesting a slight bias towards isolated modes.

A similar 2×2 table (detailed above) was then generated for each individual month (starting from March and extending through August). Figure 3 shows that CoMPS was most accurate during the spring months (March, April, and May) and least accurate during the summer months (June, July, and August). This would indicate that CoMPS provides the most skill during the spring months (when it is needed most), and is less skillful during the summer months. This decrease in accuracy during the summer could be attributed to the nature of summer time severe weather events, which are heavily influenced by mesoscale phenomena (e.g. outflow boundaries, mesoscale convective vortices). Therefore, a global model (like the GFS) will not be able to properly resolve these features, meaning the GFS output itself will contain significant errors, which conceivably translates to significant errors in CoMPS forecasts. That said, it should also

be noted that this is a very small data sample, and it would be naïve to draw any definitive conclusions regarding month-to-month accuracy trends at this time.

Another metric used to evaluate accuracy was a Linear Error Probability Space (LEPS) analysis (Figure 4). This involves the comparison of probability distribution functions (PDFs) and cumulative distribution functions (CDFs) between forecast and observation. Figure 4 shows a slight forecast bias toward isolated modes (as evident in the higher PDF and CDF values over isolated modes). The LEPS graph suggests that, on average, CoMPS is forecasting storm modes that occur about as frequently as what is observed in the atmosphere.

Numerical Model Accuracy

The two atmospheric parameters considered for assessing model accuracy are the temperature measurements at and below 100 mb and the value of one-half the maximum vertical velocity in the troposphere *w*. The mean absolute error is used to determine how much variation exists between the model forecast on which CoMPS analyzed and the model outputs taken as the "verifying observations".

$$\delta = \frac{1}{N}\sum_{i=1}^{N} |x_i - y_i| \tag{9}$$

In the above equation, *x* represents any parameter with location-specific forecast and *y* represents the observed value of the same parameter at the same location.

As detailed in the methods section, CoMPS will estimate the degree of error present in the temperature field (using the individual GEFS ensemble members) and the degree of error present in the vertical velocity field (using only the GFS vertical velocity output). The mean absolute error estimated by CoMPS was compared to what was "observed".

Figure 5 shows how mean absolute temperature error estimated by CoMPS compares to the actual mean absolute temperature error. The middle bar indicates what the GEFS ensemble members would calculate to be the mean absolute temperature error without ensemble member dressing. The rightmost bar indicates what the GEFS ensemble members would calculate to be the mean absolute temperature error *with* ensemble member dressing. The leftmost bar indicates the observed mean absolute temperature error. Based on this chart, the GEFS ensemble forecast for temperatures is "under-dispersive", meaning the uncertainty reflected on the ensemble output does not realistically depict the actual errors in temperature. Since the ensemble member dressing yields an error value that is almost identical to the observed error value, further incarnations of CoMPS that involve estimating the uncertainty of temperature should use ensemble member dressing.

Figure 5 shows how mean absolute vertical velocity error estimated by CoMPS compares to the actual mean vertical velocity error. The middle bar indicates the error CoMPS estimated without ensemble member dressing, and the rightmost bar indicates the error CoMPS estimated *with* ensemble member dressing. The leftmost bar indicates the observed mean vertical velocity error. Based on this chart, the uncertainty term for vertical velocity is overestimated, regardless

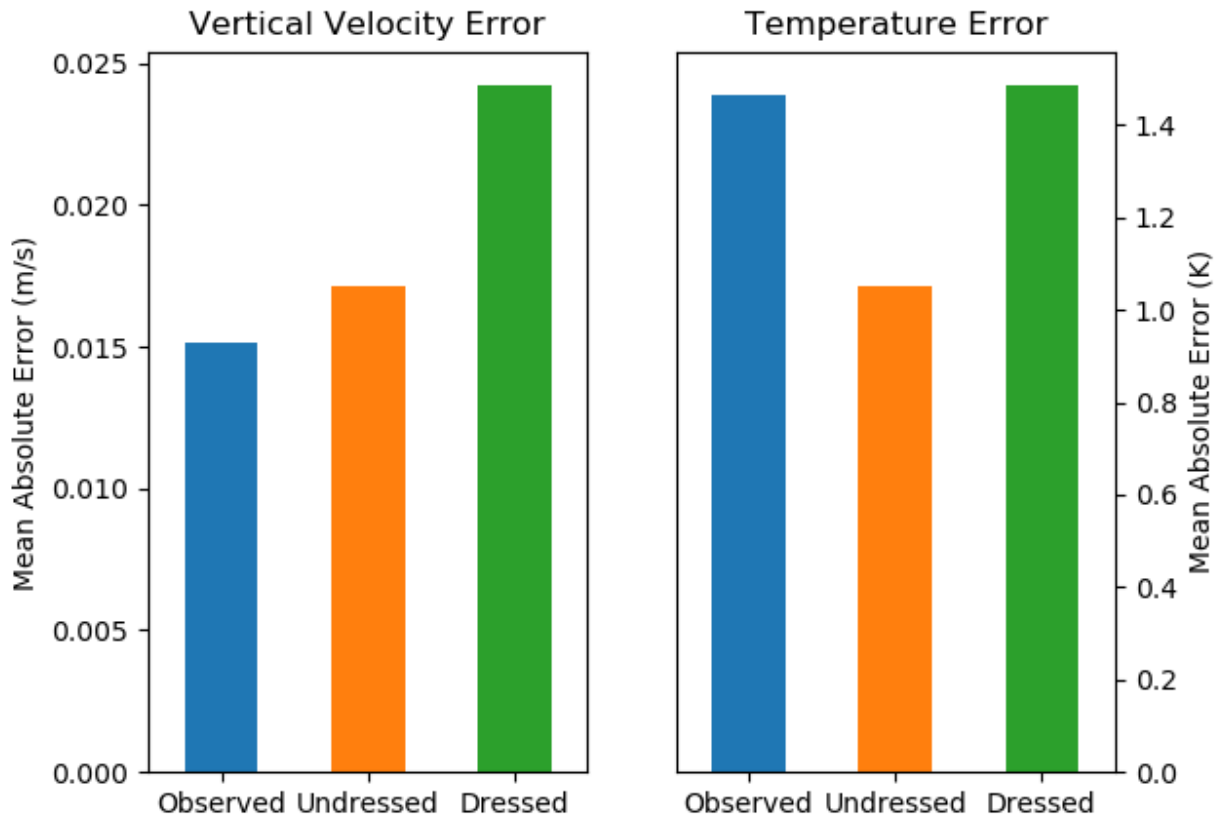

Figure 5. This figure shows how the observed model errors compare with the predicted model errors. The blue bars indicate the mean absolute error between the GFS output used in the CoMPS forecasts and the GFS output used as "verifying observations". The orange bar shows the error estimated between individual ensemble members (for temperature, on the right) and the vertical column (for vertical velocity, on the left) without any ensemble member dressing. The green bar is the orange bar with ensemble member dressing.

of ensemble member dressing. Therefore, a more accurate representation of the vertical velocity's uncertainty term might exclude the gain of 1.414.

Referring to Figure 5 again, the model forecasts for temperature at all levels at and below 100 mb were (on average) off by 1.466 K (2.639 °F). While this may seem like a small error, it is important to recall that the mean absolute error estimated on the ensemble forecasts is 1.050 K (1.890 °F). Calculating the ratio of the observed mean error to the predicted mean error yields a value of approximately 1.4 (1.466 K / 1.050 K). This implies the "observed" values for temperature frequently lie outside of the spectrum implied in the ensemble forecast, an indication of substantial error.

In the case of the representative vertical velocity estimate, the model forecasts were (on average) off by 0.015 m/s. Comparing this result to the predicted mean error of 0.017 m/s, this yields a ratio of 0.9 (0.015 m/s / 0.017 m/s). This would suggest the numerical weather models are generally producing forecasts that fall within the estimated spectrum of potential observed

values. This does not suggest the technique used to estimate vertical velocity is the best approach. However, if future work finds this to be the best possible approach for estimating a representative value for vertical velocity, the technique would yield values that most often fall within the range of possible “observations”.

Forecast Value

Given the relative lack of a third-party forecaster using CoMPS to produce forecasts, it is difficult to gauge how much value is truly added to forecasts when CoMPS is involved. However, there are two severe weather events examined in this study that indicate the potential for a significant increase in value if CoMPS were being used.

The first such case is the severe weather event on October 24th, 2021. A family of supercell thunderstorms formed in southeast Missouri in the 00Z-03Z timeframe and produced at least two long-tracked significant (EF3+) tornadoes. The CoMPS forecast for this region showed a strong signal for isolated modes throughout much of the outlook period (Figure C1), which would have highlighted increased favorability for strong tornadoes. The Storm Prediction Center (SPC) forecasted strong tornadoes, but the area drawn was notably broad (Figure C2). If the CoMPS forecast had been involved in the forecast process, a forecaster may have confined the significant tornado risk to a more specific region (excluding areas where CoMPS indicated a preference for more linear modes). Furthermore, a hindsight examination of the event suggests higher tornado probabilities should have been issued.

The second case worth discussing is the severe weather event on October 27th, 2021. A remnant squall line that formed in the Great Plains advanced eastward toward the Deep South region. CoMPS signaled potential for isolated modes during the morning hours before a full transition back to primarily linear modes (Figure C3). The SPC’s forecast discussion on the prior Day 2 outlook expressed uncertainty regarding storm mode, however, if the CoMPS forecast had been available to the forecaster, perhaps greater consideration would have been given to the potential for isolated storms to form ahead of the main line on the Day 2 outlook. Sure enough, a supercell formed in southeast Texas and produced multiple strong (EF2+) tornadoes during the morning hours.

Interpretation

Even though the accuracy of CoMPS may be lacking, it is important to remember that this model is attempting to forecast storm mode for severe weather events 96+ hours in advance. The following factors suggest that CoMPS’s inaccuracies are attributable to inaccuracies in the GFS and GEFS outputs:

- The overall forecast accuracy dropped significantly during the summer months. Summer convection is well-known for producing outflow boundaries and mesoscale convective vortices (MCVs), which are smaller-scale features a global model cannot easily resolve. Since the global model cannot resolve these features, the numerical model outputs will be inaccurate, and using these inaccurate data to

predict storm mode would result in a flawed storm mode forecast.

- The mean temperature errors imply the observed temperatures fall outside the scope of possible values indicated by the ensemble members. The individual GEFS ensemble outputs used in this study were "under-dispersive", which means the ensemble members underestimate the true uncertainty of the model's forecasts. An attempt is made to compensate for this (by using ensemble member dressing), but the fact remains that the numerical model outputs are subject to substantial errors at this forecast range, meaning it is conceivable that at least some of CoMPS's errors are due to the presence of (at times) substantial model error.
- When reproducing previous severe weather events (using observational data instead of forecast data), the median error of the CoMPS forecast was 8.0 %. Compare this to a median error of 24.4% when using forecast model outputs, and it would be valid to conclude that at least part of the forecast error is due to model inaccuracies. That said, there is still a notable degree of error when using observational data, suggesting CoMPS's governing equations can be improved.
- The evaluation of CoMPS forecasts involved a stringent examination of both the location of storm mode and the time of storm mode. This method does not account for spatiotemporal trends on the global model output. Therefore, a cold front that trends slower on subsequent model runs may produce linear modes further west and isolated modes further east. If this displacement is significant enough, isolated modes may be observed where CoMPS originally predicted linear modes. The best way to account for run-to-run model differences in the assessment of forecast accuracy is not entirely clear, but this is a factor that should be included in the forecast evaluation process.

An alternative to a purely objective evaluation process might involve a subjective evaluation by a third-party (this is discussed in greater detail in the conclusions section). Despite the unanswered questions about overall accuracy, some degree of useful accuracy has been witnessed in the spring months (March, April, and May) and at least some potential exists for added forecast value. Therefore, this first incarnation of CoMPS may prove beneficial to forecasters in an operational setting.

IV. Conclusions

The first incarnation of CoMPS has at least demonstrated a proof of concept, and additional fine tuning of the governing equations could lead to increased accuracy. CoMPS may not be ready for full-fledged operational use, but a critical evaluation of CoMPS's performance in an operational setting would be an appropriate future project. It is important to remember that forecast accuracy on its own does not automatically add value to a forecast. Therefore, the only way to assess how much value is added (or lost) in using CoMPS would be to have professional forecasters using the system on an experimental basis. One potential strategy to perform this test would be to have two teams of forecasters whose competence is all of roughly the same caliber.

One team will have access to the CoMPS forecast and the other team would not. From there, the performance of each respective team would be compared to determine how much value is added (or lost) when CoMPS is involved in the forecasting process.

Another method to evaluate the change in forecast value might involve a post-event perspective. That is, examine high-impact severe weather events where the Storm Prediction Center ideally should have issued a Day 4+ outlook area, but did not. Using this perspective, it is possible to estimate how much forecast value CoMPS *could* be providing. However, there are nuances with this approach and these nuances lie in the fact that some severe weather events cannot be predicted until a day or two in advance. As an example, consider the SPC's outlook pattern leading to the Midwest Derecho on August 10, 2020. There was no Day 4+ outlook for this particular event, the Day 3 outlook was "marginal" (level 1/5), the initial Day 2 outlook was "marginal" (level 1/5) and then upgraded to "slight" (level 2/5) on the Day 2 update, and eventually the Day 1 outlook was "moderate" (level 4/5). This pattern implies that the forecasters did not realize a derecho was imminent until the morning of the event, which therefore implies it was impossible to predict this event 4+ days in advance. In hindsight, it is easy to claim the SPC forecasters should have foreseen this high-impact event, but the information readily available at the time may have suggested this outcome was outside the realm of possibility. For this reason, the seemingly optimal and most straightforward method to evaluate the difference in forecast value would involve evaluating separate forecasting teams (some teams using CoMPS and some teams not using CoMPS) and determine which teams are producing the most accurate forecasts. If the teams using CoMPS generally produce more accurate forecasts, then there is clearly an advantage to using CoMPS. If the teams using CoMPS generally produce less accurate forecasts, then CoMPS would be providing a disadvantage.

In the interests of maintaining some degree of impartiality, the evaluation of accuracy used in this study is entirely objective. However, another direction for future work would be a third-party subjective evaluation of CoMPS forecasts. If done in an operational setting, this would give a sense of how much value is added to the forecasting process and this would better account for substantial deviations in the global numerical model outputs. To illustrate the importance of doing this, consider a hypothetical severe weather event in Arkansas where there exists a strong signal for linear modes along a cold front five days in advance. Suppose on the day of the event the parent system slows down so much that a dry line is allowed to form and produces a wave of isolated storms and the line of storms occurs many hours after it was originally expected. Objectively evaluating such an event would say that the CoMPS forecast is very inaccurate, but a subjective evaluation would account for the fact that the larger-scale pattern changed significantly leading up to the event.

CoMPS has demonstrated some degree of accuracy and is most accurate in the following scenarios:

- Severe weather events that are largely driven by the synoptic-scale features. This is a potential explanation for why the performance for CoMPS peaked in the month of April and to some extent March and May.
- Dry line driven setups in the Great Plains. Dry lines rarely changed orientation on subsequent model runs, so a dry line setup depicted several days in advance will

vaguely resemble what happens on the day of the event.

- Cold front setups in the Deep South. Cold front setups in the Great Plains were often poorly forecasted because of substantial changes in front timing and orientation on subsequent model runs.

In contrast, there are situations where CoMPS preforms poorly. These situations include events that involved:

- Outflow dominant convection (meaning the cold pool width cannot be treated as constant).
- Outflow boundaries (a storm-scale/mesoscale feature that global models cannot resolve).
- Localized weakening of inversions, which allows convection to persist after the boundary layer has stabilized (another small scale process global models cannot resolve). This usually caused CoMPS to underestimate the instability of the atmosphere and forecast isolated modes when linear modes are actually favored. This also caused CoMPS to not resolve long-lived convective lines that carried through the overnight hours into the following morning.
- Remnant mesoscale convective systems (MCSs) and their attendant mesoscale convective vortices (MCVs), another mesoscale phenomenon that global models cannot resolve.
- Topography driven events, another intricacy that global models will not resolve well.

A thorough analysis relating cold pool evolution to the ambient environment could resolve the first weakness highlighted above. Implementing a solution for the other weaknesses would not be as simple and would heavily depend on a complex statistical function. Perhaps an adaption of such concepts found in quantum mechanics could be applicable here.

The approach used in this study was rooted in a theoretical framework that used statistical methods to calibrate some of the involved quantities. Another potential approach might involve a pure machine learning method. Such an approach might also provide insight into subtle and counterintuitive details that influence storm mode. Furthermore, a finding mentioned in Dial et. al. 2010 details how time spent in a synoptic-scale boundary's initiation zone influences short-term storm mode evolution, but this is not explicitly accounted for in the governing equations for CoMPS. Other directions for future work could include:

- Evaluating CoMPS performance on other global models (e.g. the European Center Medium-range Weather Forecasting, ECMWF, model).
- Accounting for hodograph shape in the time-dependent modeling of hypothetical convective cells (the current version of CoMPS assumes a constant motion vector that follows the LCL-EL mean wind).
- Alternate schemes for classifying storm mode (linear vs. isolated), such schemes may include a decision tree and fuzzy logic.

- Directly relating the parameters P_0 (initiation probability) and Δs (storm width) to the ambient environment. As an example, it is well-known that Dixie Alley can often host supercells that are very small in comparison to supercells that form over the Plains. The smaller value of Δs would tend toward a stronger preference for isolated modes. Therefore, using a specific and appropriate value for Δs (as opposed to a generic value based on a national mean) should theoretically improve the accuracy of storm mode forecasts.
- Alternate schemes for lifting hypothetical parcels (accounting for drag, entrainment, pressure perturbations, and strong wind shear destroying weak updrafts or enhancing updrafts). This would improve the accuracy of P_0 (initiation probability) and thereby provide a better representation for the quantity of storms that are expected.

Furthermore, the predictive strategy for non-frontal convection hinged on a purely stochastic model with a partial foundation in the theoretical framework. Using an entirely empirical approach might improve the storm mode forecast accuracy. This could be accomplished by acquiring radar data of non-frontal convection that is purely isolated or purely linear and determining the quantity of cells and the mean width of each cell shown. From there, an empirical equation could be used to probabilistically predict storm mode based on the parameters P_0 (initiation probability) and Δs (convective cell width).

Other avenues for future work might include alternative methods for evaluating CoMPS forecasts. One underlying challenge with this study was the presence of multiple potential sources for substantial error (be it the numerical model outputs, the governing equations, the observational data, or the objective analysis algorithms). The technique used in this study involved discretizing the forecast and observation to account for wide margins of error, but other and more insightful techniques (such as those found in Ebert et. al. 2013, Murphy 1991, and Mason and Weigel 2009) may be applicable.

Even though significant work has already been done to develop this first incarnation of a second-order model (i.e. a model on top of a model), there is an immense amount of potential for future work to improve, fine-tune, and evaluate this first incarnation of CoMPS. Though the original intent was for CoMPS to operate on global model outputs, a sufficiently accurate version of CoMPS could also provide a second opinion to what CAMs predict.

References

Bitsa, E., H. A. Flocas, J. Kouroutzoglou, G. Galanis, M. Hatzaki, G. Latsas, I. Rudeva, I. Simmonds, 2021: A Mediterranean Cold Front Identification Scheme Combining Wind and Thermal Criteria, *International Journal of Climatology*, 1-14, https://doi.org/10.1002/joc.7208.

Dial, G. L., J. P. Racy, R. L. Thompson, 2010: Short-Term Convective Mode Evolution along Synoptic Boundaries, *Weather and Forecasting*, **25**, 1430-1446, https://doi.org/10.1175/2010WAF2222315.1.

Dixon, M., G. Weiner, 1993: TITAN: Thunderstorm Identification, Tracking, Analysis, and Nowcasting - A Radar-based Methodology, *Journal of Atmospheric and Oceanic Technology*, **10**, 785-797, https://doi.org/10.1175/1520-0426(1993)010<0785:TTITAA>2.0.CO;2.

Ebert, E., and Coauthors, 2013: Progress and Challenges in Forecast Verification, *Meteorological Applications*, **20**, 130-139, 10.1002/met.1392.

European Centre for Medium-Range Weather Forecasts (ECMWF), 2017: Experts to Explore Global Modelling at Resolutions Under 10 km. Accessed 25 Oct 2021, https://www.ecmwf.int/en/about/media-centre/news/2017/experts-explore-global-modelling-resolutions-under-10-km.

Gerard, L., J.-F. Geleyn, 2005: Evolution of a Subgrid Deep Convection Parameterization in a Limited-Area Model With Increasing Resolution, *Quarterly Journal of the Royal Meteorological Society*, **131**, 2293-2312, doi: 10.1256/gj.04.72.

Govett, Mark, n. d.: Radiosonde Database Access. National Oceanic and Atmospheric Administration, Accessed 4 Nov 2020, https://ruc.noaa.gov/raobs/.

Helmus, J. J. and S. M. Collis: JORS 2016, doi: 10.5334/jors.119

Ivanova, A. R., 2013: The Tropopause: Variety of Definitions and Modern Approaches to Identification, *Russian Meteorology and Hydrology*, **38**, 808-817, doi: 10.3103/S1068373913120029.

Kawabata, T., G. Ueno, 2020: Non-Gaussian Probability Densities of Convection Initiation and Development Investigated Using a Particle Filter with a Storm-Scale Numerical Weather Prediction Model, *Monthly Weather Review*, **148**, 3-20, https://doi.org/10.1175/MWR-D-18-0367.1.

Lewis, H. W., 2009: A Robust Method for Tropopause Altitude Identification Using GPS Radio Occultation Data, *Geophysical Research Letters*, **36**, 1-5, https://doi.org/10.1029/2009GL039231.

Lock, N. A., A. L. Houston, 2014: Empirical Examination of the Factors Regulating Thunderstorm Initiation, *Monthly Weather Review*, **142**, 240-258, https://doi.org/10.1175/MWR-D-13-00082.1.

Mason, S. J., A. P. Weigel, 2009: A Generic Forecast Verification Framework for Administrative Purposes, *Monthly Weather Review*, **137**, 331-349, https://doi.org/10.1175/2008MWR2553.1.

Meyer, B., J. O. Haerter, 2020: Mechanical Forcing of Convection by Cold Pools: Collisions and Energy Scaling, *Journal of Advances in Modeling Earth Systems*, **12**, 1-20, https://doi.org/10.1029/2020MS002281.

Murphy, A. H., 1990: Forecast Verification: Its Complexity and Dimensionality, *Monthly Weather Review*, **119**, 1590-1601, https://doi.org/10.1175/1520-0493(1991)119<1590:FVICAD>2.0.CO;2.

National Centers for Environmental Information, n. d.: Global Forecast System. National Oceanic and Atmospheric Administration, Accessed 9 Mar 2021, https://www.ncei.noaa.gov/products/weather-climate-models/global-forecast.

National Oceanic and Atmospheric Administration, 2021: Historical Level II Radar Data. Amazon Web Services, Accessed 4 Sep 2020, https://s3.amazonaws.com/noaa-nexrad-level2/index.html.

National Oceanic and Atmospheric Administration, n. d.: NOAA Operational Model Archive and Distribution System., Accessed 25 Mar 2021, 3 Apr 2021, 7 Apr 2021, 19 Apr 2021, 20 Apr 2021, 21 Apr 2021, 30 Apr 2021, 5 May 2021, 24 May 2021, 6 Jun 2021, 5 Jul 2021, 7 Aug 2021, 10 Aug 2021, 17 Aug 2021, 22 Aug 2021, 25 Aug 2021, 12 Sep 2021, 6 Oct 2021, 21 Oct 2021, 22 Oct 2021, https://nomads.ncep.noaa.gov.

Pan, L. L., L. C. Paulik, S. B. Honomichl, L. A. Munchak, J. Bian, H. B. Selkirk, H. Vömel, 2013: Identification of the Tropical Tropopause Transition Layer Using the Ozone-Water Vapor Relationship, *Journal of Geophysical Research: Atmospheres*, **119**, 3586-3599, https://doi.org/10.1002/2013JD020558.

Peter, J. R., M. J. Manton, R. J. Potts, P. T. May, S. M. Collis, L. Wilson, 2015: Radar-Derived Statistics of Convective Storms in Southeast Queensland, *Journal of Applied Meteorology and Climatology*, **54**, 1985-2008, https://doi.org/10.1175/JAMC-D-13-0347.1.

Pinto, J., C. Mueller, S. Weygandt, J. Wilson, 2006: Fusing Observation- and Model-Based Probability Forecasts for the Short Term Prediction of Convection. *12th Conference on Aviation Range and Aerospace Meteorology*, Atlanta, GA, American Meteorological Society, P11.7, https://ams.confex.com/ams/Annual2006/techprogram/paper_105453.html

Rao, D. N., M. V. Ratnam, V. J. Rao, S. K. Mehta, D. Nath, S. G. Basha, 2007: Identification of Tropopause Using Bending Angle Profile From GPS Radio Occultation (RO): A Radio Tropopause, *Geophysical Research Letters*, **34**, 1-7, https://doi.org/10.1029/2007GL029709.

Schwartz, C. S., M. Wong, G. S. Romine, R. A. Sobash, K. R. Fossell, 2020: Initial Conditions for Convection-Allowing Ensembles over the Conterminous United States, *Monthly Weather Review*, **148**, 2645-2669, https://doi.org/10.1175/MWR-D-19-0401.1.

Smith, B. T., R. L. Thompson, J. S. Grams, C. Broyles, H. E. Brooks, 2012: Convective Modes for Significant Severe Thunderstorms in the Contiguous United States. Part I: Storm Classification and Climatology, *Weather and Forecasting*, **27**, 1114-1135, https://doi.org/10.1175/WAF-D-11-00115.1.

Storm Prediction Center, n. d.: Storm Prediction Center Severe Weather Events Archive. Accessed 19 Oct 2021, https://www.spc.noaa.gov/exper/archive/events.

Stratman, D. R., M. C. Coniglio, S. E. Koch, M. Xue, 2013: Use of Multiple Verification Methods to Evaluate Forecasts of Convection from Hot- and Cold-Start Convection-Allowing Models, *Weather and Forecasting*, **28**, 119-138, https://doi.org/10.1175/WAF-D-12-00022.1.

Wang, X., C. H. Bishop, 2004: Improvement of Ensemble Reliability With A New Dressing Kernel, *Quarterly Journal of the Royal Meteorological Society*, **131**, 965-986, doi: 10.1256/gj.04.120.

Weckwerth, T. M., D. B. Parsons, 2006: A Review of Convection Initiation and Motivation for IHOP_2002, *Monthly Weather Review*, **134**, 5-22, https://doi.org/10.1175/MWR3067.1.

Xia, P., Y. Shan, S. Ye, W. Jiang, 2021: Identification of Tropopause Height with Atmospheric Refractivity, *Journal of the Atmospheric Sciences*, **78**, 3-16, https://doi.org/10.1175/JAS-D-20-0009.1.

Zan, B., Y. Yu, J. Li, G. Zhao, T. Zhang, J. Ge, 2019: Solving the Storm Split-Merge Problem - A Combined Storm Identification, Tracking Algorithm, *Atmospheric Research*, **281**, 335-346, https://doi.org/10.1016/j.atmosres.2018.12.007.

Acknowledgements

Dr. Patrick Marsh (Storm Prediction Center Science Support Branch Chief) for providing the idea and motivation for this project.

Richard Thompson (Storm Prediction Center Lead Forecaster) for reviewing the overall approach.

Dr. Cameron Homeyer (University of Oklahoma School of Meteorology Professor) for providing accommodations that made this research possible.

Dr. Xuguang Wang for the recommendation for using ensemble member dressing to assimilate model data.

Dr. Michael Richman for providing possible classification strategies for linear and isolated modes (including the ones mentioned in the conclusions section).

Dr. Harold Brooks for providing forecast evaluation strategies for CoMPS forecasts.

The staff at Pivotal Weather for recommending the NOMADS resource for model data.

Appendix A: Figures

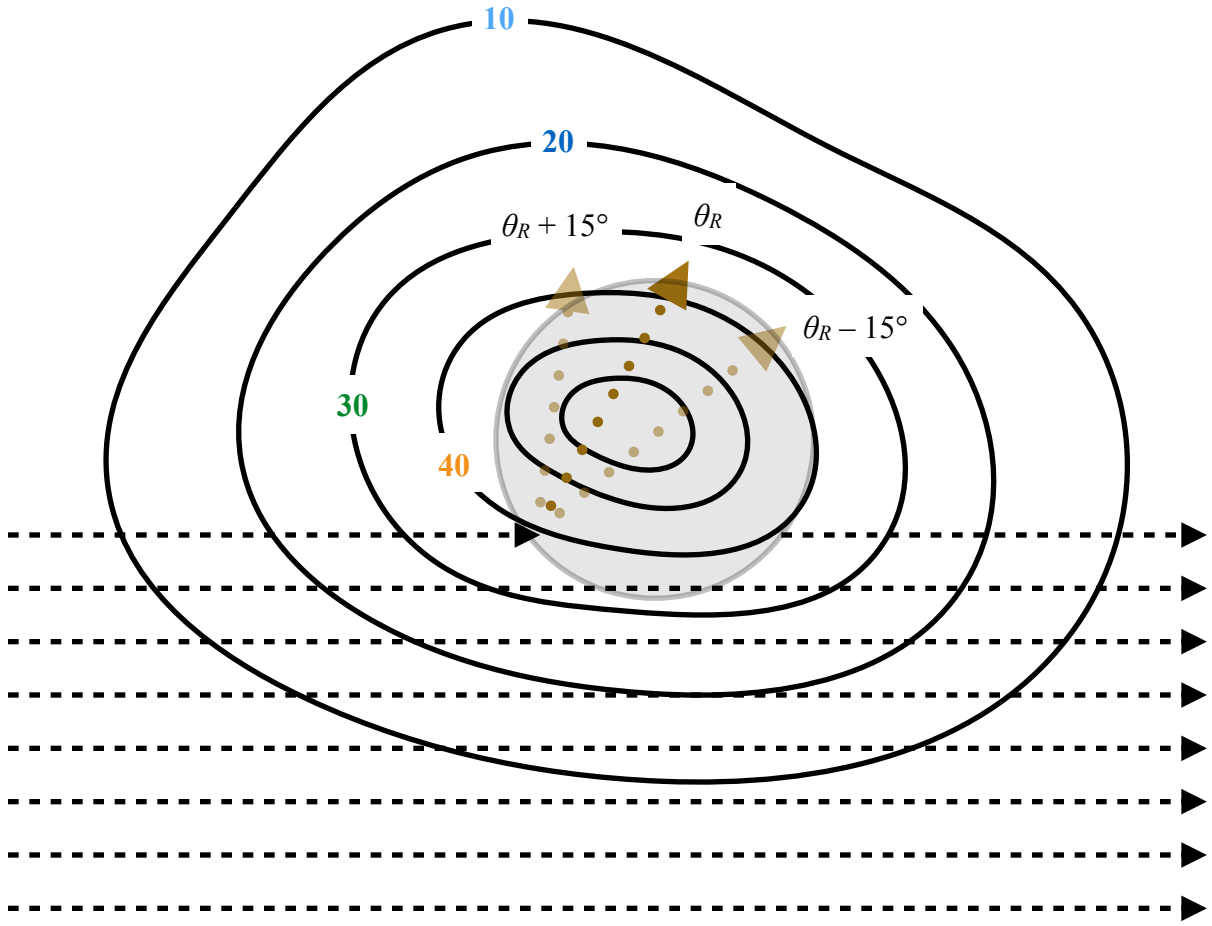

Figure A1. This figure shows how the objective radar analysis algorithm identifies and estimates the width of a cell using base radar reflectivity. The contours represent base reflectivity values. The dashed arrows represent the algorithm scanning grid points from left to right. The dark brown arrow represents the direction of ∇R and the faded brown arrows show the angular domain covered by the algorithm. The inferred quasi-circular cold pool is shown in gray.

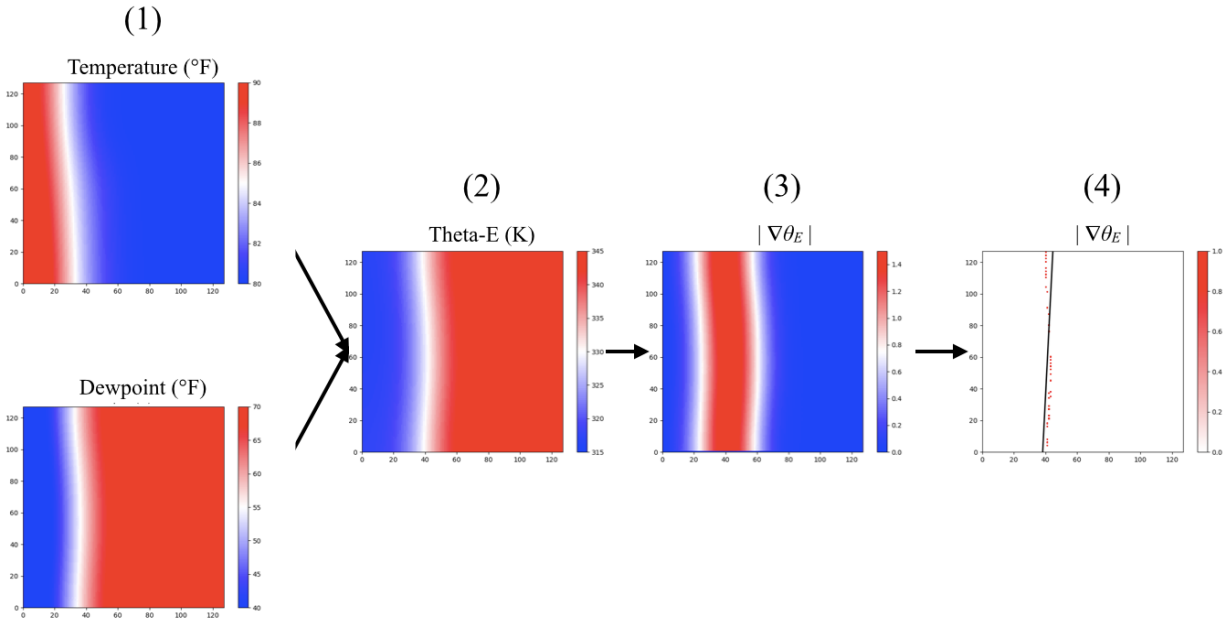

Figure A2. This figure illustrates the algorithm used to identify the orientation of well-defined boundaries, in this case a dry line. Start with the temperature and dewpoint values on an isobaric surface (1), then use these fields to calculate θ_E (2), then calculate the value of $|\nabla\theta_E|$ (3), then highlight values of $|\nabla\theta_E|$ that are "significant" (4), (detailed in the algorithm's description). The angle of the best-fit line then becomes the boundary's orientation (angle).

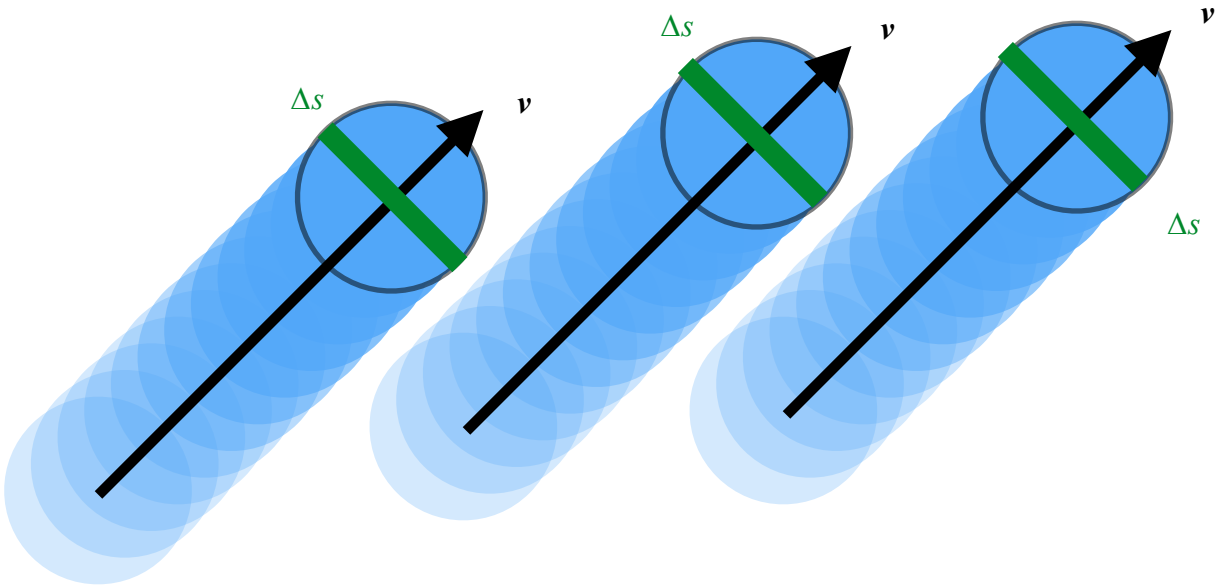

Figure A3. This figure shows a schematic, representing the swath of cooled air traced out by convective cells with cold pool width Δs (green) moving with velocity $\boldsymbol{v}$ (black).

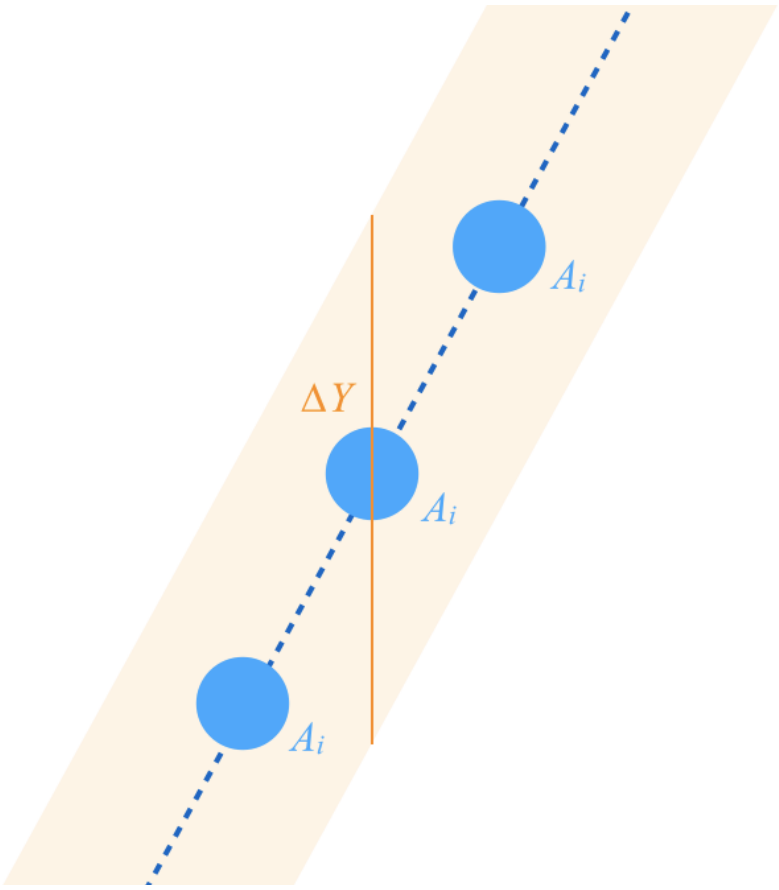

Figure A4. This figure visualizes how CoMPS initiates a hypothetical array of convective cells, provided a "well-defined" boundary exists. The dark blue dashed line represents the axis of the boundary, and the light blue circles represent the initial cold pools of width Δs. The orange parallelogram represents the initiation zone.

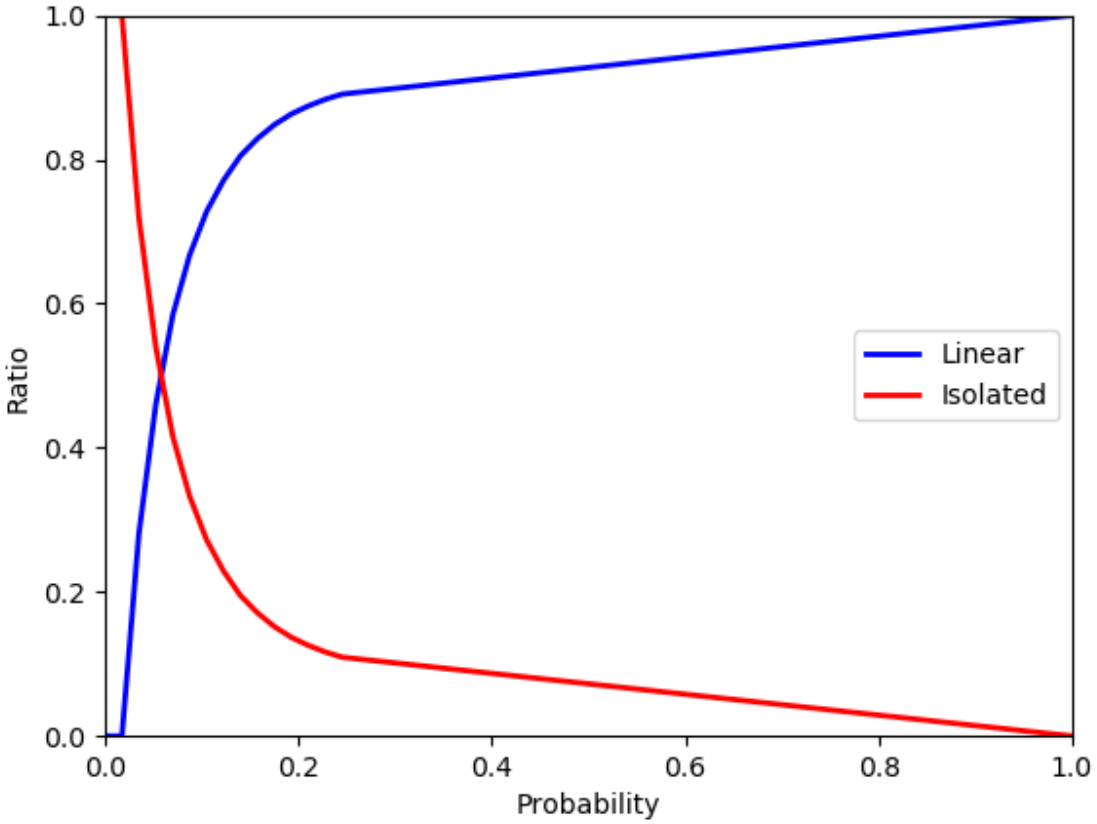

Figure A5. This figure shows the stochastic function that is used to estimate storm mode when there exists no "well-defined" boundary.

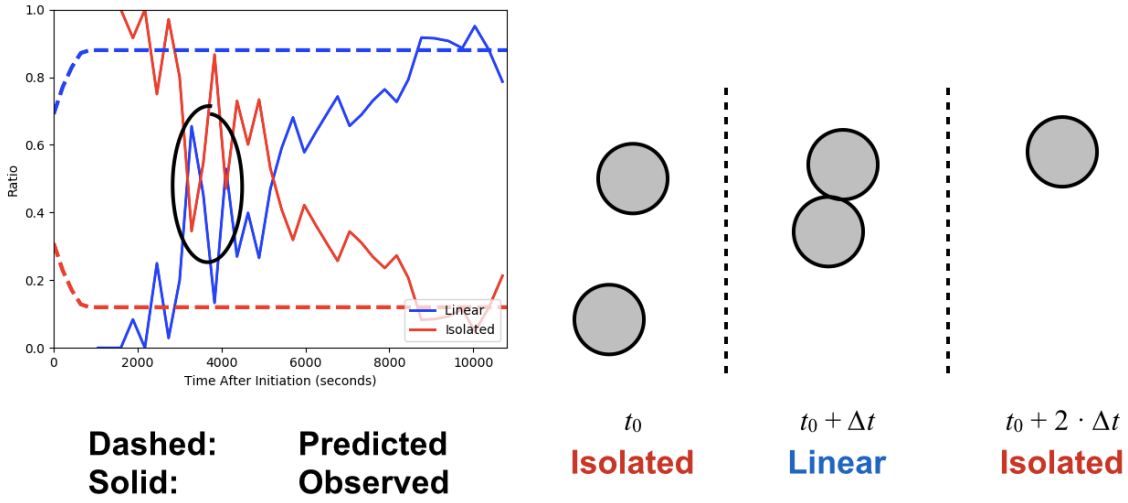

Figure A6. This figure illustrates what happens with the objective radar analysis algorithm when cell mergers are being observed. Notice in the circled region there are several sudden decreases of (increases of) isolated modes (linear modes). This is due to individual cells moving closer together, therefore being identified as "linear". After the merge is complete, the analysis reverts back to the original values of isolated modes and linear modes.

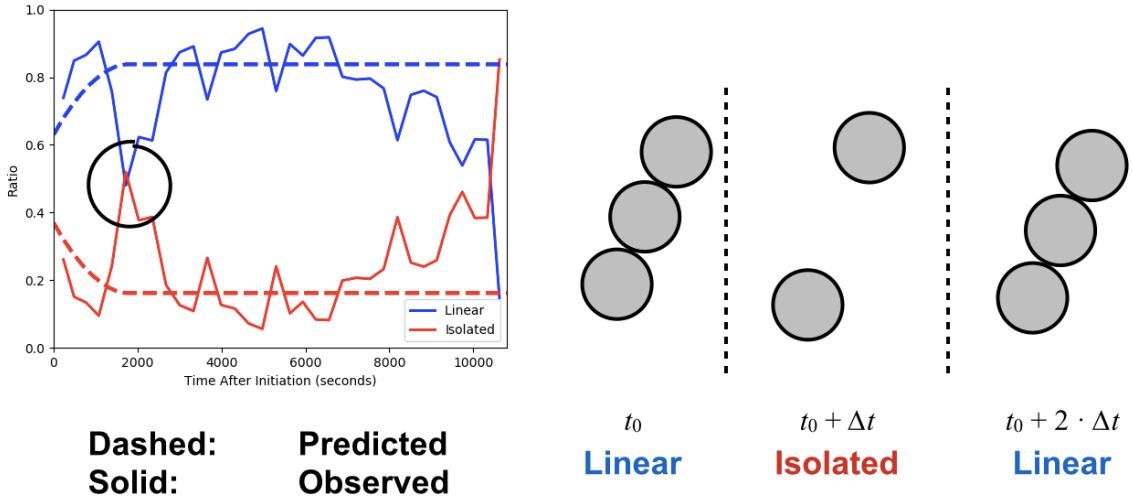

Figure A7. Same as Figure A4, but showing what happens when individual cells embedded within line experience transient weakening. If an individual cell begins to yield weaker radar returns, the objective algorithm will miss the weak return until it re-intensifies on a later scan.

Appendix B: Tables

Table B1. The stochastic function values plotted on Figure A3.

Initiation Probability P_0	Stochastic Function Value (Linear)	Stochastic Function Value (Isolated)
0.00000	0.00000	1.00000
0.01752	0.00000	1.00000
0.03504	0.28044	0.71956
0.05256	0.46038	0.53962
0.07008	0.58416	0.41584
0.08760	0.66764	0.33236
0.10512	0.72791	0.27209
0.12264	0.77129	0.22871
0.14016	0.80521	0.19479
0.15767	0.82910	0.17090
0.17519	0.84827	0.15173
0.19271	0.86311	0.13689
0.21023	0.87424	0.12576
0.22775	0.88341	0.11659
0.24527	0.89064	0.10936
1.00000	1.00000	0.00000

Table B2. This table shows all of the severe weather events with a CoMPS forecast. Most of the excluded events were discarded because the severe weather risk was below Enhanced (level 3/5). May 2nd, 2021 was excluded because the Enhanced Risk on this date was not for the original Day 4 outlook area.

Event Date	Outlook Day Number	Risk	Status
March 28th, 2021	4	Enhanced	Included
April 7th, 2021	5	Enhanced	Included
April 10th, 2021	4	Enhanced	Included
April 23rd, 2021	5	Enhanced	Included
April 24th, 2021	5	Enhanced	Included
April 27th, 2021	7	Slight	Excluded
May 2nd, 2021	4	Enhanced	Excluded
May 3rd, 2021	5	Enhanced	Included
May 8th, 2021	4	Enhanced	Included
May 27th, 2021	4	Enhanced	Included
June 10th, 2021	5	Moderate	Included
July 9th, 2021	5	Enhanced	Included
August 10th, 2021	4	Enhanced	Included
August 13th, 2021	4	Slight	Excluded
August 20th, 2021	4	Slight	Excluded
August 22nd, 2021	4	Slight	Excluded
August 28th, 2021	4	Enhanced	Included

Appendix C: Select Event Database

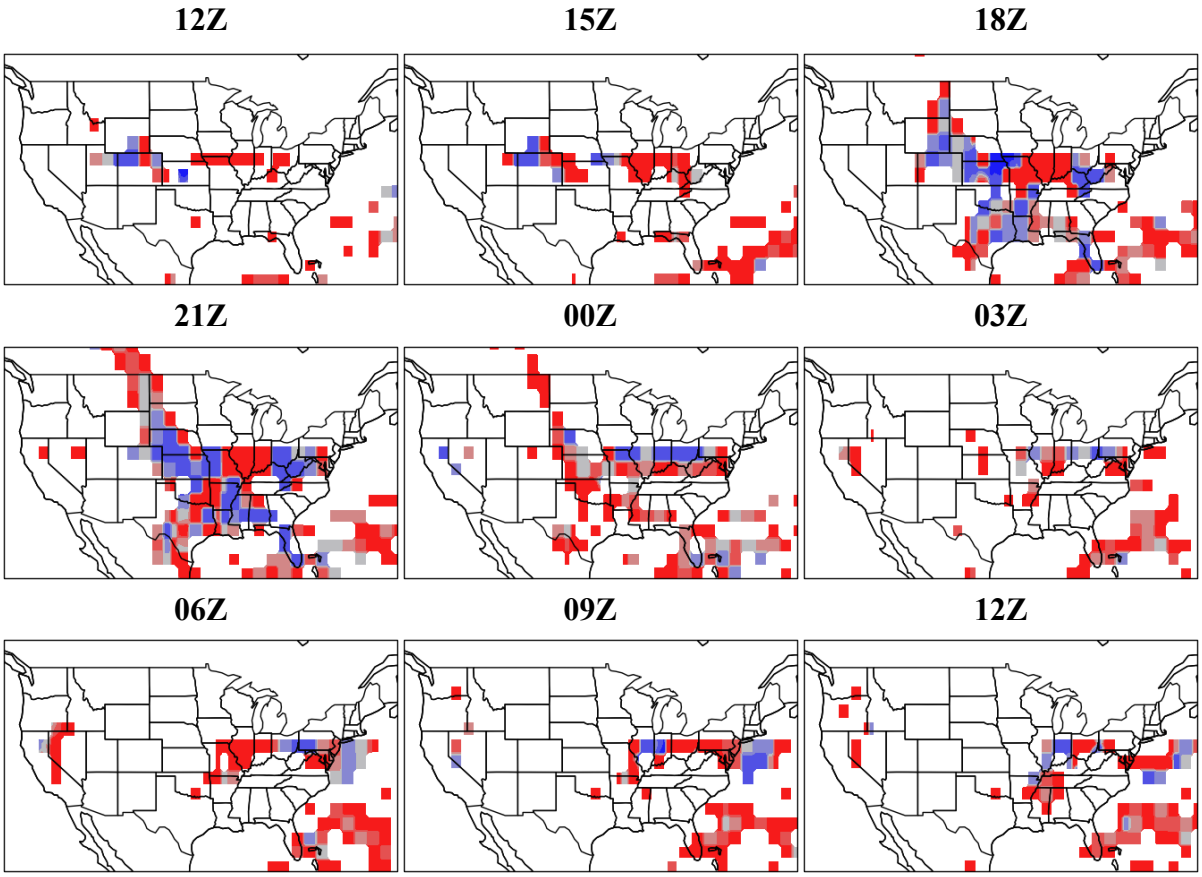

Figure C1. This figure shows the CoMPS forecast for the selected severe weather event on October 24th, 2021 (red is isolated, blue is linear, gray is mixed modes). Between 00Z and 03Z, a family of discrete supercells formed and produced long-track significant tornadoes in southeast Missouri, where CoMPS showed a strong and persistent signal for isolated modes (96 hours in advance).

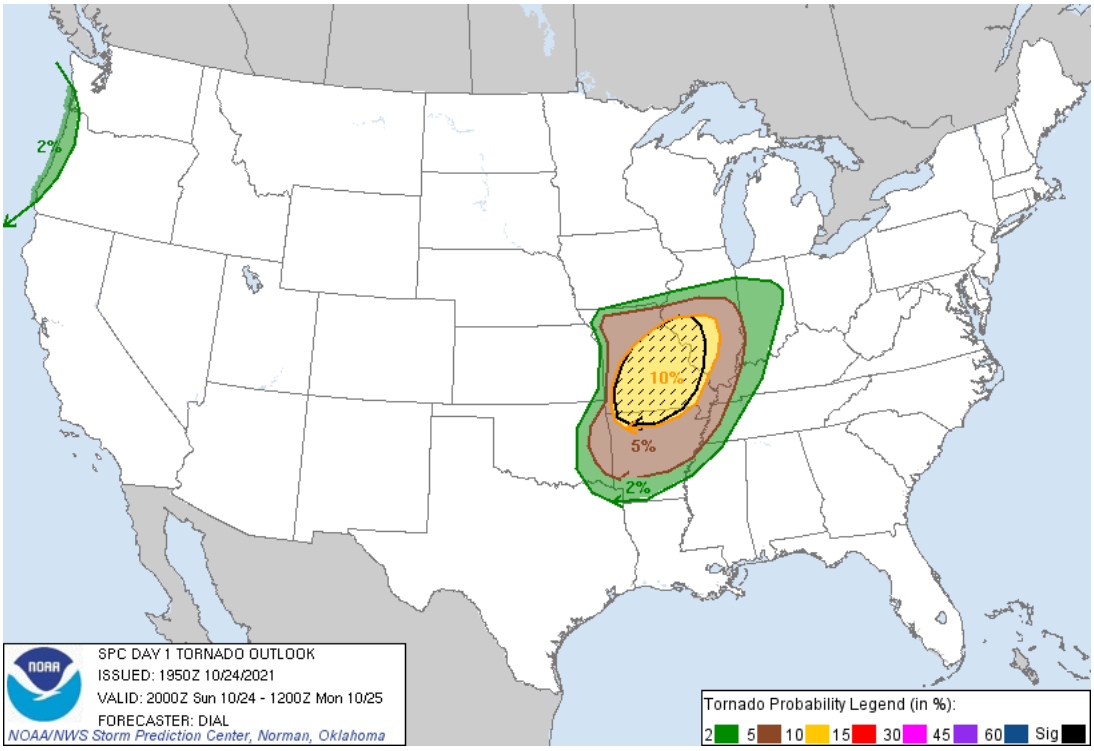

Figure C2. This figure shows the Storm Prediction Center's tornado forecast on the 20Z outlook for October 24th, 2021. Compare this to Figure C1 and note how the broad hatched area (a forecast for significant, EF2+, tornadoes) includes areas where linear modes were forecasted by CoMPS. This shows how (in this specific case) CoMPS could have improved the forecasting process since all of the significant tornadoes occurred in southeast Missouri (where CoMPS persistently forecasted isolated modes).

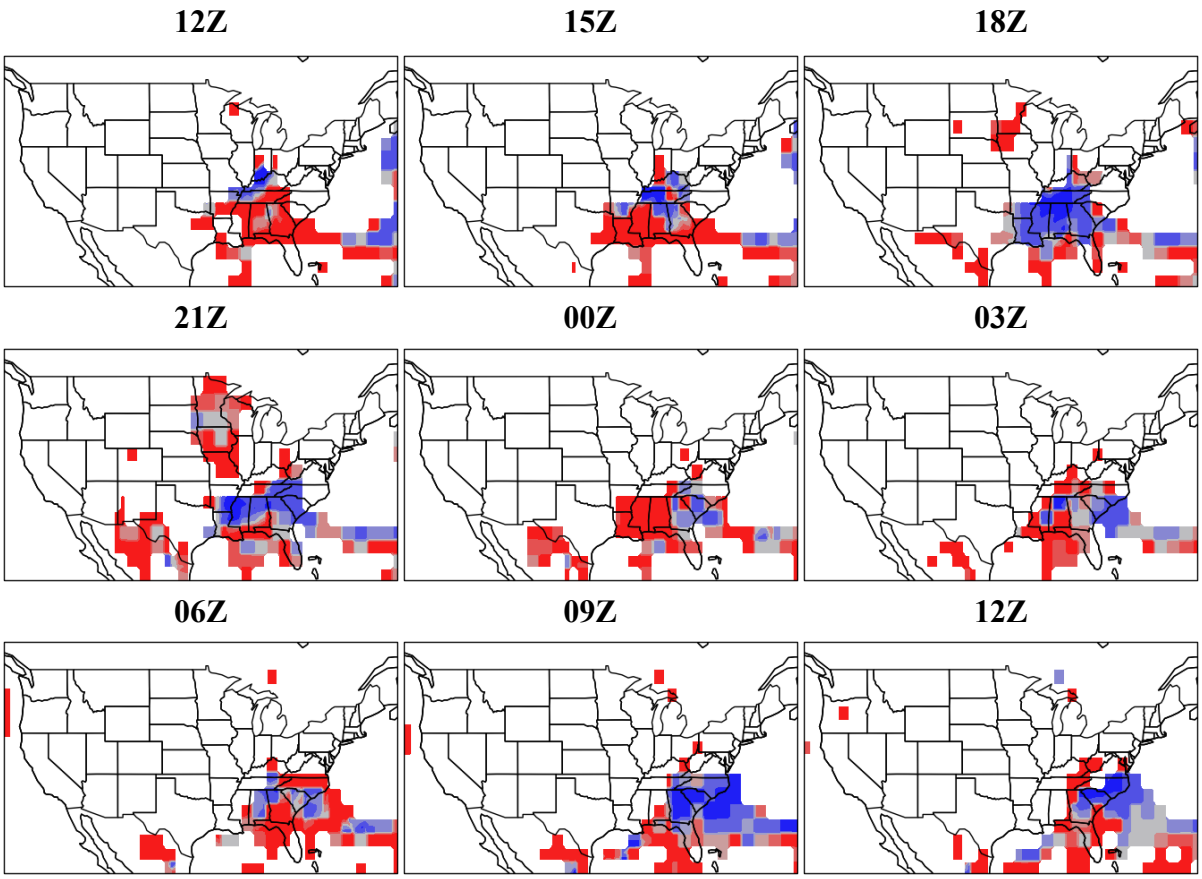

Figure C3. This figure shows the CoMPS forecast for the selected severe weather event on October 27th, 2021 (red is isolated, blue is linear, gray is mixed modes). Around 15Z, a supercell formed in southeast Texas and dropped a series of tornadoes (including some EF2+) as it approached the Louisiana border. This coincides very well with the CoMPS forecast around the same time, which strongly signals isolated modes. The squall line that carried through the overnight hours was not resolved by the GFS, so it is initially absent on the CoMPS forecast in the morning hours.